$$H_\tau(\phi) = H(\phi - \tau). \quad \cdots\cdots (9)$$

This relationship is appropriate when there is a delay between $P(t)$ and $V_0(t)$ in Eq. (8) [29].

## 3. Results

**3.1 Spontaneous firing** The model presented in this study shows many features observed in whole-cell patch-clamp recording for DA cells in rat midbrain slices. A typical waveform of membrane voltage in spontaneous firing of DA cells of the substantia nigra pars compacta (SNc) is illustrated in Fig. 1A. Membrane voltage of spontaneous firing in the model is shown in Fig. 1B ($I_{app}$=0 nA/cm$^2$). It is known that the voltage hyperpolarization immediately after spikes is deeper in DA cells than pyramidal cells in the neocortex; this is represented by the model. In addition, the characteristic slow oscillations were observed in subthreshold membrane voltage after blocking of sodium currents by treatment of DA cells in brain slices with tetrodotoxin (TTX). This observation was also mimicked by reducing the conductance of the voltage-dependent sodium channel in the model (e.g., $g_{Na}$=0 S/cm$^2$). The action-potential waveforms from the experiment and the model showed similar spike amplitude and width. Furthermore, the first and second derivatives of the two waveforms also showed similar time courses, which indicated that the model successfully mimicked the shape of action potentials.

**3.2 Bifurcation diagram** To examine oscillatory phenomena of the model in more detail, a one-parameter ($I_{app}$) bifurcation diagram was computed (Fig. 2). The oscillation emerges through a supercritical Hopf bifurcation when the externally injected current went beyond a point at $I_1$. The threshold of the firing cannot be theoretically defined in the supercritical Hopf bifurcation case. However, in this analysis, oscillations where the membrane voltage went beyond +40 mV

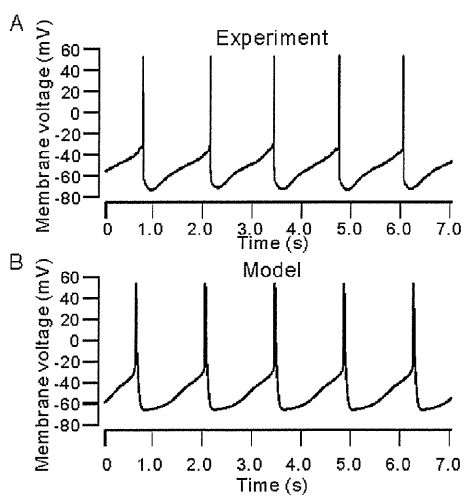


Fig. 1. Comparison of membrane voltage traces. Membrane voltage recorded from a spontaneously active dopaminergic neuron in a rat midbrain slice is shown in A. Membrane voltage of the model can mimic spontaneous firing of rat dopaminergic neurons in whole-cell patch-clamp recording in B.

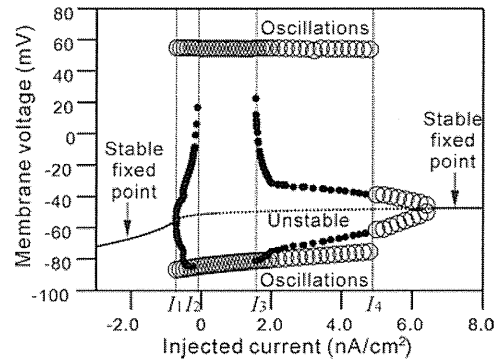


Fig. 2. One-parameter ($I_{app}$) bifurcation diagram. Solid and dotted lines show stable and unstable fixed points, respectively. Open and filled circles show maximum or minimum voltages in superthreshold and subthreshold oscillations, respectively. The oscillation emerges through a Hopf bifurcation point at $I_1$ and ends at $I$=6.51; $I_1$=−0.716, $I_2$ =−0.173, $I_3$ =1.56, and $I_4$=4.69.

were considered as action potentials. In addition to superthreshold oscillations (i.e., action potentials), subthreshold oscillations were observed in two regimes of the intervals [$I_1$, $I_2$] and [$I_3$, $I_4$]. In the interval between $I_2$ and $I_3$, superthreshold oscillations were only observed, and the oscillations corresponded to the spontaneous regular firing shown in Fig. 1B.

**3.3 Hyperpolarization-activated current regulates firing frequency** In DA neurons in the midbrain, HCN channels are expressed from early postnatal development stages (data not shown here). The HCN channels are activated in hyperpolarized membrane voltage, and the current $I_h$ was actually observed under −70 mV in the voltage-clamp recording. In current-clamp recording, the current component constructs a characteristic membrane-voltage response of so called "sag" (Fig. 3A(a)), and the present model can mimic the voltage response (Fig. 3A(b)). A computational simulation of the model revealed that the conductance ($g_h$) of HCN channels regulated the firing frequency of spontaneous activity in DA neurons, as illustrated in Fig. 3B. As the conductance increased, the firing rate was monotonically increased until $g_h$=0.12 and over that value, the rate was decreased. Moreover, the rate was thereafter disrupted discontinuously around $g_h$=0.15. Over that value, the firing frequency slowed down, because regular firing of action potentials was changed into the mixture of action potentials and subthreshold oscillations. The result indicated that HCN channels regulate not only firing frequency but also the types of oscillations (i.e., regular action potentials or the mixture of sub- and superthreshold oscillations).

**3.4 Phase-resetting curves** Next, to understand the relationship between the amount of HCN channel expression and phase changes in periodic cycles of regular spiking, phase-resetting curves (PRCs) were investigated. In Fig. 4A, PRCs with four different $g_h$ values are illustrated. If there was no HCN channel expression (i.e., $g_h$=0), the PRC was monophasic, and there was no delayed phase regions in the curve. In contrast, as the conductance was increased, a delayed phase appeared and PRCs were biphasic (e.g., $g_h$=0.15). In addition, with increasing conductance, the amplitude in the advanced phase was decreased, and the amplitude in the delayed phase and the portion to the

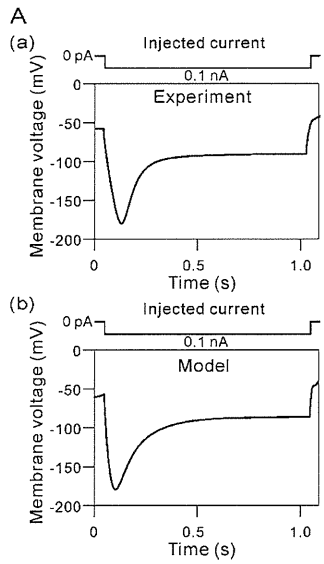


A, Comparison of membrane voltage responses.
In response to hyperpolarizing (negative) direct current injection, membrane voltage traces in a representative dopaminergic cell (a) and the present model (b) are shown. The amplitude of the injected current was 0.1 nA in both cases.

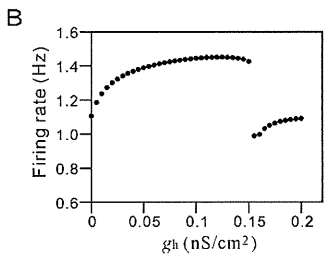


B, A relationship between spontaneous firing frequency and the maximum conductance ($g_h$) of the HCN channel.
Fig. 3. Electrical properties in the computational model of dopaminergic neurons.

whole phase was increased. In Fig. 4B, the relationships between advanced and delayed phases with $g_h$ are illustrated. The results indicated that the shape of PRCs was regulated by the HCN channel conductance.

### 3.5 Stability of the coupled phase-equation model

Finally, to understand the relationship between the amount of HCN channel expression and the stability of the model in gap junction-coupled DA neurons, $H$ functions in Eq. (8) and their derivatives were numerically investigated. For four different values of $g_h$, the $H$ functions and their derivatives are shown in Figs. 5A and B. In all of the $H$ functions, stable fixed points are located at $\phi = 0$ (Fig. 5A), which means that the phase difference $\phi = \theta_1 - \theta_2$ between the two phase-oscillators can eventually converge to zero after a transient period. Therefore, over a transient period, two oscillators are phase-locked and synchronized. However, if there exists a relatively longer time delay $\tau$ to the period in the oscillation cycle, a different case happens. This corresponds to a case where, for example, there was

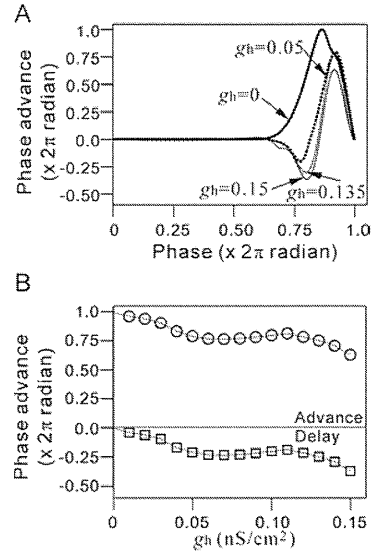


Fig. 4. HCN channel conductance ($g_h$) dependency in phase resetting curves. Phase resetting curves with four different values of HCN maximum conductance $g_h$ are shown; $g_h$=0.1, 0.05, 0.135, and 0.15 in A. The curves are normalized by the sum of maximum phase advance and minimum phase delay. The relationships of phase advance (○) and delay (□) vs. $g_h$ are illustrated in B.

a time delay between a spike initiation zone and a gap-junction site. In such a case, each stable fixed point cannot be always located at $\phi = 0$ because of Eq. (9) (Fig. 5B). Moreover, if the time delay is over 10% of the period of unperturbed oscillators, the oscillation can be unstabilized (i.e., $dH(0)/d\phi<0$ in Fig. 5B). Furthermore, for each $\phi$, the area at which $dH(0)/d\phi < 0$ against $g_h$ is shown and illustrated by gray color in Fig. 5C. As explained above, the time delay shifted the gray area downward. In addition, the result shown in Fig. 5C indicated that, as $g_h$ was increased, the region at which $dH(0)/d\phi < 0$ was reduced, so that the time delay $\tau$ induced less instability.

In summary, the HCN channel conductance regulated the extent of stability of the coupled oscillators of the model. In addition, if the HCN channels were expressed and the time delay $\tau$ was equal to zero or less than 10% of the unperturbed oscillation, the two oscillators were always synchronized and phase-locked.

## 4. Discussion

DA cells are spontaneously active in both *in vivo* and *in vitro* recordings [1,4]. It is known that adult DA neurons are $Ca^{2+}$-dependent autonomous pacemakers; that is, their basal activity is intrinsically driven by voltage-dependent L-type $Ca^{2+}$ channels [4]. Voltage-dependent $Ca^{2+}$ channels are multimeric proteins in which the pore-forming α-subunit is the principal determinant of gating and pharmacology. L-type $Ca^{2+}$ channels in brain neurons have one of two α-subunits: $Ca_v1.2$ or $Ca_v1.3$. However, genetic deletion of $Ca_v1.2$ and $Ca_v1.3$ $Ca^{2+}$ channels did not stop pacemaking in DA neurons. In contrast, HCN channels

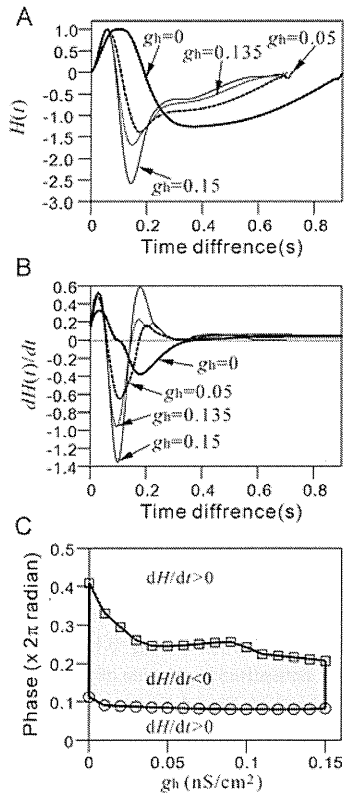


Fig. 5. Stability analysis of the coupled-phase oscillator model. In four different values of $g_h$ (i.e., $g_h$=0.1, 0.05, 0.135, and 0.15), $H(t)$ functions are shown in A. Here, $t = T_0\phi / (2\pi)$ in the $H$ functions, where $T_0$ is the period of the uncoupled oscillators. For convenience, $H(t)$ was normalized by the maximum value of each function. Similarly, in the four different values of $g_h$, the derivatives of $H(t)$ are illustrated in B. Borderlines between positive and negative derivatives of $H(t)$ are illustrated against each $g_h$ in C.

widely partner voltage-dependent $Na^+$ channels in pacemaking [30]. Recently, Chan et al. reported that, in DA neurons from $Ca_v1.3$ knockout mice, HCN channels were absolutely critical, because an antagonist for these channels completely stopped pacemaking [31]. It is also known that, in DA neurons taken from younger mice (less than three weeks old), HCN channels were also very important in maintaining normal spiking rates [31]. However, as the switch to $Ca_v1.3$-channel–dependent pacemaking evolved, these channels became less important. Therefore, little is known about the functional role of HCN channels in adult DA neurons.

In this study, the conductance-based Hodgkin–Huxley type DA cell model was first constructed on the basis of reported results and data recorded from DA cells in rat midbrain slices. The model mimicked membrane-voltage waveforms in spontaneous firing (Fig. 1B) and responses to hyperpolarizing current injection (Fig. 3Ab). Next, we focused, in particular, on the functional role of HCN channels. As shown in the Results section, if the HCN channel conductance ($g_h$) was increased, the firing rate was monotonically increased until some value, and over the value, the rate was decreased (Fig. 3B). The result indicated that there can be an optimal value of $g_h$ for maximizing spontaneous firing rate in DA neurons.

Second, we numerically analyzed the stability of oscillations in response to direct current injection and obtained the bifurcation diagram (Fig. 2B). The bifurcation analysis of the model revealed that there was a complex structure for spontaneous firing and for evoked firing even in response to a simple direct current injection. In some parameter ranges, a mixture of action potentials and subthreshold oscillations was observed. A variety in the amount of HCN channel expression could provide more complexity in the bifurcation structure owing to the discontinuity of the relationships between firing rate and HCN channel conductance (Fig. 3B).

Third, to gain some insight into synchronized phenomena in gap junction-coupled DA neurons, a weakly coupled phase-equation model of two identical DA neurons was derived after numerically computing PRCs of regular firing using the conductance-based model. The analysis revealed that the shape of PRCs tightly depended on HCN channel conductance, and a HCN-channel conductance-dependent transition from monophasic to biphasic PRCs was found. The transition was critical for the maintenance of synchronization and phase-locking of the coupled oscillators. In addition, to examine synchronized phenomena among DA cells, a stability analysis of synchronization between coupled oscillators was applied to the model. The results indicated that HCN channels can regulate not only the frequency of firing and subthreshold oscillations in membrane voltage but also the extent of synchronization and desynchronization among DA cells. Thus, in regards to the main autonomous-pacemaking role of adult DA neurons, HCN channels in younger aged animals are similar to L-type $Ca^{2+}$ channels [31]. However, we show here that HCN channels can also contribute to the maintenance of synchronization in coupled oscillations and stability of synchronization regions in gap-junction coupling between DA neurons.

In many neurons of the central nervous system, hormones and neurotransmitters that elevate cyclic adenosine monophosphate (cAMP) levels facilitate activation of $I_h$ by shifting the voltage values for half-maximal activation ($V_{0.5}$) to more positive values and by accelerating the opening kinetics. It has been shown that, in DA neurons, the acceleration of the opening kinetics with cAMP can be attributed to the shift in voltage dependence of activation [32]. Thus, in the presence of high cAMP concentrations, $I_h$ channel opening is faster and more complete than at low cAMP levels. As it is also known that HCN channels are expressed by SNc and VTA DA neurons, they are exquisitely sensitive to allosteric regulation by cAMP [32]. Because SNc DA neurons expressed $Ca^{2+}$-inhibited isoforms of the enzyme that produces cAMP, it is plausible that rising intracellular $Ca^{2+}$ concentrations dampen cAMP synthesis, leading to a shift in HCN gating in a relatively longer time scale. Hence, the activation of HCN channels can be regulated by the cAMP level and the $Ca^{2+}$ concentration [31].

## 5. Conclusion

To understand the functional role of HCN channels, we constructed a conductance-based model of DA cells. To test the validity of the model, spontaneous firing and membrane voltage responses evoked by hyperpolarizing current injection were compared with those from actual DA cells of midbrain slices in

*in-vitro* recordings. The model analysis revealed that HCN channels can regulate not only the frequency of firing and subthreshold oscillations in membrane voltage but also the extent of synchronization and desynchronization among DA cells. Hence, HCN channels not only in premature DA cells but also in adult DA cells have special functional roles in the regulation and maintenance of cooperative firing through gap-junction coupling between DA cells.

## Appendix A

**A.1** The transient $Na^+$ current ($I_{Na}$) is described by

$$I_{Na} = g_{Na} m_{Na}^3 n_{Na} (V - E_{Na}),$$

and the voltage-dependent activation and deactivation functions and time-constant functions are as follows:

$$m_\infty(V) = 1.0 / \left[\exp\left(-(V + 18.0)/7.41\right) + 1.0\right]$$
$$\tau_m(V) = 0.0369 + 0.0791 \exp\left(-(V + 21.2)^2 / 1403.8\right)$$
$$n_\infty(V) = 1.0 / \left[\exp\left((V + 47.8)/3.96\right) + 1.0\right]$$
$$\tau_n(V) = 2.02 + 50.9 \exp\left(-(V + 56.5)^2 / 296.8\right)$$

**A.2** The delayed rectifier $K^+$ current ($I_K$) is described by

$$I_K = g_K m_K^4 (V - E_K),$$

and the voltage-dependent activation and time-constant functions are as follows:

$$m_\infty(V) = 1.0 / \left[\exp\left(-(V + 34.4)/8.99\right) + 1.0\right]$$
$$\tau_m(V) = 0.201 + 14.4 \exp\left(-(V - 17.2)^2 / 1084\right)$$

**A.3** The A-type potassium current ($I_A$) is described by

$$I_A = g_A m_A^3 n_A (V - E_K),$$

and the voltage-dependent activation and deactivation functions and time-constant functions are as follows:

$$m_\infty(V) = 1.0 / \left[1.0 + \exp\left(-(V + 62.4)/16.0\right)\right]$$
$$\tau_m(V) = 1.62 + 7.99 \exp\left(-(V + 102.2)^2 / 3952\right)$$
$$n_\infty(V) = 1.0 / \left[1.0 + \exp\left(-(V + 83.9)/5.66\right)\right]$$
$$\tau_n = 26.8$$

**A.4** The M-type potassium current ($I_M$) is described by

$$I_M = g_M m_M (V - E_K),$$

and the voltage-dependent activation and time-constant functions are as follows:

$$m_\infty(V) = 1.0 / \left[\exp\left(-(V + 41.5)/5.47\right) + 1.0\right]$$
$$\tau_m(V) = 87.5 + 172 \exp\left(-(V + 25.4)^2 / 735.0\right)$$

**A.5** The h-type cation current ($I_h$) is described by

$$I_h = g_h m_h (V - E_h),$$

and the voltage-dependent activation and time-constant functions are as follows:

$$m_h(V) = 1.0 / \left[1.0 + \exp\left((V + 69.9)/10.5\right)\right]$$
$$\tau_m(V) = 320 + 1850 \exp\left(-(V + 81.0)^2 / 18.1\right).$$

**A.6** In the model, four different types of calcium currents are included. The L-type calcium current ($I_{CaL}$) is described by

$$I_{CaL} = g_{CaL} m_{CaL} (V - E_{Ca}),$$

and the voltage-dependent activation and time-constant functions are as follows:

$$m_\infty(V) = 1.0 / \left[1.0 + \exp\left(-(V + 31.4)/5.34\right)\right]$$
$$\tau_m(V) = 4.7 + 11.7 \exp\left(-(V + 54.2)^2 / 1034\right).$$

The N-type calcium current ($I_{CaN}$) is described by

$$I_{CaN} = g_{CaN} m_{CaN} n_{CaN} (V - E_{Ca}),$$

and the voltage-dependent activation and time-constant functions are as follows:

$$m_\infty(V) = 1.0 / \left[\exp\left(-(V + 24.4)/5.47\right) + 1.0\right]$$
$$\tau_m(V) = 0.0306 + 18.0 \exp\left(-(V + 34.5)^2 / 720.0\right)$$
$$n_\infty(V) = 1.0 / \left[\exp\left((V + 54.5)/5.34\right) + 1.0\right]$$
$$\tau_n(V) = 49.8 + 450 \exp\left(-(V + 70.5)^2 / 501.4\right)$$

The P-type calcium current ($I_{CaP}$) is described by

$$I_{CaP} = g_{CaP} m_{CaP} n_{CaP} (V - E_{Ca}),$$

and the voltage-dependent activation and time-constant functions are as follows:

$$m_\infty(V) = 1.0 / \left[\exp\left(-(V + 25.9)/5.38\right) + 1.0\right]$$
$$\tau_m(V) = 0.569 + 10.4 \exp\left(-(V + 38.1)^2 / 765.6\right)$$
$$n_\infty(V) = 1.0 / \left[\exp\left((V + 64.9)/1.87\right) + 1.0\right]$$
$$\tau_n(V) = 14.5 + 389 \exp\left(-(V + 75.5)^2 / 21.5\right)$$

The T-type calcium current ($I_{CaT}$) is described by

$$I_{CaT} = g_{CaT} m_{CaT} n_{CaT} (V - E_{Ca}),$$

and the voltage-dependent activation and time-constant functions are as follows:

$$m_\infty(V) = 1.0 / \left[\exp\left(-(V + 62.4)/1.19\right) + 1.0\right]$$
$$\tau_m(V) = 12.0 + 65.0 \exp\left(-(V + 68.0)^2 / 36.0\right)$$
$$n_\infty(V) = 1.0 / \left[\exp\left((V + 75.3)/2.77\right) + 1.0\right]$$
$$\tau_n(V) = 10.0 + 50.0 \exp\left(-(V + 72.0)^2 / 100\right)$$

**A.7** The Calcium-activated potassium SK current ($I_{SK}$) is described by

$$I_{SK} = g_{SK}([Ca^{2+}]_i)(V - E_K).$$

**Acknowledgements**. This work was supported by the Funding Program for Next Generation World-Leading Researchers (NEXT program), Precursory research for Embryonic Science and Technology (PRESTO), Japan Science and Technology Agency (JST) and Grant-in-Aid for Scientific Research (B) and Exploratory Research, the Ministry of

Education, Culture, Sports, Science and Technology (MEXT).

(Manuscript received Jan. 00, 2000, revised May 00, 2000)

## References

(1) Schultz W. Getting formal with dopamine and reward. *Neuron* 2002; **36(2)**:241–263.

(2) Brozoski TJ, Brown RM, Rosvold HE, Goldman PS. Cognitive deficit caused by regional depletion of dopamine in prefrontal cortex of rhesus monkey. *Science* 1979; **205(4409)**:929–932.

(3) Graybiel AM, Aosaki T, Flaherty AW, Kimura M. The basal ganglia and adaptive motor control. *Science* 1994; **265(5180)**:1826–1831.

(4) Liss B, Roeper J. Individual dopamine midbrain neurons: functional diversity and flexibility in health and disease. *Brain Research Reviews* 2008; **58(2)**:314–321.

(5) Wahl-Schott C, Biel M. HCN channels: structure, cellular regulation and physiological function. *Cellular and molecular life sciences* 2009; **66(3)**: 470–494.

(6) Tateno T. A small-conductance $Ca^{2+}$-dependent $K^+$ current regulates dopamine neuron activity: a combined approach of dynamic current clamping and intracellular imaging of calcium signals. *Neuroreport* 2010; **21(10)**: 667–674.

(7) Hodgkin AL, Huxley AF. A quantitative description of membrane current and its application to conduction and excitation in nerve. *Journal of Physiology* 1952; **117(4)**:500–544.

(8) Amini B, Clark JW, Canavier CC. Calcium dynamics underlying pacemaker-like and burst firing oscillations in midbrain dopaminergic neurons: a computational study. *Journal of Neurophysiology* 1999; **82(5)**: 2249–2261.

(9) Kuznetsov AS, Kopell NJ, Wilson CJ. Transient high-frequency firing in a coupled-oscillator model of the mesencephalic dopaminergic neuron. *Journal of Neurophysiology* 2006; **95(2)**: 932–947.

(10) Yang F, Feng L, Zheng F, Johnson SW, Du J, Shen L, Wu CP, Lu B. GDNF acutely modulates excitability and A-type $K^+$ channels in midbrain dopaminergic neurons. *Nature Neuroscience* 2001; **4(11)**: 1071–1078.

(11) Koyama S, Appel SB. A-type $K^+$ current of dopamine and GABA neurons in the ventral tegmental area. *Journal of Neurophysiology* 2006; **96(2)**: 544–554.

(12) Liss B, Roeper J. ATP-sensitive potassium channels in dopaminergic neurons: transducers of mitochondrial dysfunction. *News in physiological sciences* 2001; **16**: 214-217.

(13) Brown DA, Adams PR. Muscarinic suppression of a novel voltage-sensitive $K^+$ current in a vertebrate neurone. *Nature* 1980; **283(5748)**: 673-676.

(14) Lacey MG, Calabresi P, North RA. Muscarine depolarizes rat substantia nigra zona compacta and ventral tegmental neurons in vitro through M1-like receptors. *Journal of Pharmacology and Experimental Therapeutics* 1990; **253(1)**: 395-400.

(15) Koyama S, Appel SB. Characterization of M-current in ventral tegmental area dopamine neurons. *Journal of Neurophysioogyl* 2006; **96(2)**: 535-543.

(16) Mercuri NB, Bonci A, Calabresi P, Stefani A, Bernardi G. Properties of the hyperpolarization-activated cation current $I_h$ in rat midbrain dopaminergic neurons. *European Journal of Neuroscience* 1995; **7(3)**: 462-469.

(17) Liu Z, Bunney EB, Appel SB, Brodie MS. Serotonin reduces the hyperpolarization-activated current ($I_h$) in ventral tegmental area dopamine neurons: involvement of 5-HT2 receptors and protein kinase C. *Journal of Neurophysiology* 2003; **90(5)**: 3201-3212.

(18) Durante P, Cardenas CG, Whittaker JA, Kitai ST, Scroggs RS. Low-threshold L-type calcium channels in rat dopamine neurons. *Journal of Neurophysiology* 2004; **91(3)**: 1450-1454.

(19) Kang Y, Kitai ST. Calcium spike underlying rhythmic firing in dopaminergic neurons of the rat substantia nigra. *Neuroscience Research* 1993; **18(3)**: 195-207.

(20) Silva NL, Pechura CM, Barker JL. Postnatal rat nigrostriatal dopaminergic neurons exhibit five types of potassium conductances. *Journal of Neurophysiology* 1990; **64(1)**: 262-272.

(21) Kohler M, Hirschberg B, Bond CT, Kinzie JM, Marrion NV, Maylie J, Adelman JP. Small-conductance, calcium-activated potassium channels from mammalian brain. *Science* 1996; **273(5282)**: 1709-1714.

(22) Wilson CJ, Callaway JC. Coupled oscillator model of the dopaminergic neuron of the substantia nigra. *Journal of Neurophysiology* 2000; **83(5)**: 3084-3100.

(23) Ermentrout B. *Simulating, Analyzing, and Animating Dynamical Systems: A Guide to XPPAUT for Researchers and Students:* Society for Industrial Mathematics Philadelphia; 2002.

(24) Winfree AT. *The Geometry of Biological Time:* Springer: New York; 2001.

(25) Tateno T, Robinson HP. Phase resetting curves and oscillatory stability in interneurons of rat somatosensory cortex. *Biophys J* 2007; **92(2)**: 683-695.

(26) Williams TL, Bowtell G. The calculation of frequency-shift functions for chains of coupled oscillators, with application to a network model of the lamprey locomotor pattern generator. *Journal of Computational Neuroscience* 1997; **4(1)**: 47-55.

(27) Kopell N, Ermentrout GB. Oscillator death in systems of coupled neural oscillators. *SIAM Journal on Applied Mathematics* 1990; **50(1)**: 125-146.

(28) Hoppensteadt FC, Izhikevich EM. *Weakly Connected Neural Networks*. Springer. New York; 1997.

(29) Kopell GB, Ermentrout N. Mechanisms of phase-locking and frequency control in pars of coupled neural oscillators, in *Handbook of Dynamical Systems*. B. Fiedler, ed., Berlin: Elesevier, 2002, pp. 3-54.

(30) Surmeier DJ, Mercer JN, Chan CS. Autonomous pacemakers in the basal ganglia: who needs excitatory synapses anyway? *Curremt Opinion in Neurobiology* 2005; **15(3)**: 312-318.

(31) Chan CS, Guzman JN, Ilijic E, Mercer JN, Rick C, Tkatch T, Meredith GE and Surmeier DJ. 'Rejuvenation' protects neurons in mouse models of Parkinson's disease. *Nature* 2007; **447(7148)**: 1081-1086.

(32) Zolles G, Klocker N, Wenzel D, Weisser-Thomas J, Fleischmann BK, Roeper J, Fakler B. Pacemaking by HCN channels requires interaction with phosphoinositides, *Neuron* 2006;**52(6)**: 1027–1036.

**Takashi Tateno** (Member) received B.E., M.E., and Ph.D. degrees in

Biophysical Engineering from the Osaka University, Japan, in 1992, 1994, and 1999, respectively. In 1994, he joined NTT Basic Research Laboratories, where he was engaged in research in the field of neuroscience. Since 1999, he has been with Osaka University. From 2002 to 2004, he was a visiting researcher at the Department of Physiology, University of Cambridge, U.K. Since 2007, he has been an associate professor of Graduate School of Engineering Science, Osaka University.

論　文

# 中脳ドーパミン細胞における形態発達の特徴と受動的膜モデルの一構成法

正員　舘野　高*,**

# Morphological Properties in Dopaminergic Neurons of the Rat Midbrain during Early Developmental Stages and One Numerical Approach to Passive-Membrane Modeling

Takashi Tateno*,**, Member

In this study, I aim to understand morphological changes in dopaminergic neurons of the rat midbrain during early developmental stages and their computational properties in the dendrites. To this end, firstly, I measured morphological details of dopaminergic neurons using an immunochemical double-staining technique. In the viewpoint of the Rall's equivalent-cylinder model, secondly, I tested if the data satisfied one of conditions (3/2 power law) of the Rall's model. On the basis of the experimental data, I next investigated if some branches in the individual dendrites had special selectivity in efficient passive propagation of membrane potentials between the branches of individual cells and different cells. The results show that the Rall's 3/2 power law was not satisfied in many branch points and that among branches of each dendrite, specific selectivity in efficient propagation was not found. In addition, I note an implementation method in which the finite element method is applied to one-dimensional cable model of dendrites and give some numerical examples.

キーワード：樹状突起，ドーパミン細胞，有限要素法，免疫化学染色法

**Keywords**：dendrite, dopaminergic neuron, finite element method, immunochemical staining

## 1. はじめに

大脳基底核は大脳皮質下核であり，解剖学的には，線条体とその他の複合核（淡蒼球，黒質，視床下核）に大別される。大脳基底核は，体性運動機能に関与し，行動や情動を支配する辺縁系を統合する部位と考えられる[1]。近年，特に，逐次系列の行動障害やパーキンソン病などの運動障害[2]，および，強化学習[3]の関連から，線条体と並んで，黒質の局所回路網とドーパミン作動性細胞が注目されている。

パーキンソン病の特徴である運動症状を引き起こす原因は，黒質緻密部にあるドーパミン作動性（DA）神経細胞数の減少であると考えられている。しかし，何故DA細胞が傷害を受けやすいかは現時点で明らかではないが，細胞内のカルシウム濃度上昇が主要な因子であるとの説がある[4]。近年，Chanらは，DA細胞が$Ca^{2+}$チャネルに依存して律動的活動を維持しており，この依存性が加齢と共に強くなることを示した[5]。また，高血圧や脳卒中の治療に使われるカルシウム拮抗薬のイスラジピンを投与することで，成人の神経細胞を若年の神経細胞と同様に，$Na^{+}$/HCNチャネル依存性に逆戻りさせることが可能であることが知られている。特に，パーキンソン病のマウスモデルでは，この「若返り」がDA細胞を保護することから，この方法で病気の進行を遅らせる可能性が示唆されている[5]。さらに，DA細胞は，樹状突起から神経伝達物質ドーパミンを放出し，その効果は抑制性であることから，活動に依存して自己抑制をかける仕組みをもつことが知られている[6]。

上記のような理由から，DA神経細胞のイオンチャンル特性とその細胞形態を含めたダイナミクスを詳細に理解することは，パーキンソン病などの脳疾患にとって重要である。近年，このような背景から，DA神経細胞の数理モデルがいくつか提案されている[7][8]。しかし，その多くは現象論的事実を単純な数式で置き換えたものに過ぎず，実験データに基づいておらず，新たな実験の検証に堪え得るものではない。また，実験で得られた細胞形態データを詳細に再現するモデルも現時点では存在しない。

Rallは1950年代から始まる先駆的な研究によって，樹状突起の電気的特性をモデル化する理論的枠組みを与えた[9]。特に，Rallは枝分かれする樹状突起を受動的膜として膜電位

* 科学技術振興機構　さきがけ
〒332-0012　埼玉県川口市本町4-1-8
PRESTO, JST
4-1-8, Honcho, Kawaguchi, Saitama 332-0012
** 大阪大学大学院　基礎工学研究科
〒560-8531　大阪府豊中市待兼山町1-3
Graduate School of Engineering Science, Osaka University
1-3, Machikaneyama-cho, Toyonaka-shi, Osaka 560-8531

を解析的に扱う線形ケーブル理論[9]と樹状突起を非線形興奮性膜として膜電位を数値的に計算するコンパートメントモデル[10]を脊髄の運動ニューロンに応用した[9][11]。

本研究では，黒質，および，腹側被蓋野のドーパミン細胞の発達に伴う変化を，その特徴と機能の両面から理解することを目指しており，その中で，特に黒質のDA細胞の形態的特徴を研究の対象としている。本研究では，まず，細胞形態の初期発達を理解するために，二重免疫染色法を用いて，生後3日目，および，15日目の2つのステージにおけるラット中脳黒質のDA細胞の形態を計測した。そして，それらの細胞形態の特徴を定量化した。ラットは生後10日前後で聴覚末梢系の細胞が分化し，生後13日前後の開眼によって視覚が機能発達を始める。また，この発達ステージで細胞間の電気的シナプスが急激に減少することが知られており[5]，それに伴う神経回路網のダイナミクスの変化の解析は興味深い問題である。次に，Rallのモデル化の観点から神経細胞形態の受動的特性を理解するために，実際に計測した細胞形態データに基づき，DA細胞がRallの等価シリンダ (Rall's equivalent cylinder) モデルの条件を満たすか否かを検討した。さらに，有限要素法を応用した樹状突起モデルの一構成法の計算機による実装方法と，その方法の具体的な応用例を述べる。

## 2. 方　法

**〈2·1〉 Rallの等価シリンダモデルと幾何学的比**　以下の2つの条件が満たされるとき，分岐した樹状突起を1本の電気的等価シリンダとして扱うことができることをRallは示した。(条件1) 分岐した樹状突起の半径の3/2乗の和は分岐前の半径の3/2乗に等しい (Rallの3/2乗則)。(条件2) 細胞体から全ての分岐の端までの電気緊張性距離 (electrotonic distance) は等しい。(条件3) 全ての樹状突起の終端の境界条件は等しい[13]。この条件下で，ある細胞の樹状突起に対して，それを等価変換したモデルをRallの等価シリンダモデルとよぶ。運動ニューロンでは (条件1) のRallの3/2乗則はほぼ満たされているが，(条件2) は満たされておらず，分岐の端までの電気緊張性距離は細胞によって様々であることが知られている[14]。

細胞体からの距離 $x$ における等価シリンダの半径は，樹状突起の分岐点後の半径 $r_j$ を使って，関係式：

$$r_{eq}(x)=\left[\sum_j r_j(x)^{3/2}\right]^{2/3} \quad \cdots\cdots(1)$$

を用いて計算する。また，Rallらは幾何学的比 (geometric ratio, GR) を

$$\mathrm{GR}=\sum_j r_j^{3/2}/r_a^{3/2} \quad \cdots\cdots(2)$$

と定義した[15]。ここで，$r_a$ と $r_j$ は各々電位が伝播する前後の樹状突起の半径を表す。ここでは，$r_a$ が細胞体により近い位置とする。Y字型の分岐点において，GR≠1の場合には，インピーダンス不整合が生じる。したがって，膜電位伝播において振幅が減衰するために，伝搬効率が悪い場合 (GR>1) と効率が良い場合 (GR<1) が生じる。

**〈2·2〉 スライスの作成と単一細胞記録**　全ての実験は大阪大学動物実験委員会の承認を受け，大阪大学動物実験規定に基づき行った。実験には生後3日齢，および，生後15日齢のラット (Wistar rat, 日本SLC) を使用した。ラットに吸引麻酔を施した後，素早く脳を取り出した。脳を適当な形に切り出した後に，スライス用ステージに固定し周囲を冷却しながらslicing solution (125 mM NaCl, 2.5 mM KCl, 26 mM $NaHCO_3$, 1.25 mM $NaH_2PO$, 25 mM Glucose, 4 mM $MgCl_2$, 0.1 mM $CaCl_2$, saturated with 95% $O_2$ and 5% $CO_2$) に浸した。その後，ビブラトーム (DTK-3000, D.T.K., Kyoto, Japan) を用いて，300 μm厚の冠状断面切片を作成した。作成した脳スライスは組織回復のために常温の人工脳髄液 (ACSF; 125 mM NaCl, 2.5 mM KCl, 26 mM $NaHCO_3$, 1.25 mM $NaH_2PO$, 25 mM Glucose, 4 mM $MgCl_2$, 0.1 mM $CaCl_2$, saturated with 95% $O_2$ and 5% $CO_2$) に1時間浸した。その後，脳スライスを記録用チャンバーに移動した。そして，36℃のACSFを2.0 ml/minで灌流させた。ステージ固定型正立顕微鏡 (BX61WI, Olympus社) を用いて近赤外微分干渉像の観察を行い，ガラス電極を使って細胞膜を破り，電極内液を細胞中に拡散させた。使用したガラス電極の抵抗は7.0±1.0 MΩであった。また，電極内液には，0.2%のbiocytinを加えた。

**〈2·3〉 免疫組織化学法**　ガラス電極内液を細胞に拡散させた後に，脳スライスを4%パラホルムアルデヒドで一晩固定した。固定した脳スライスをリン酸緩衝生理食塩水で洗浄し，冷凍した際の組織の損傷を防ぐため15%スクロース溶液で30分，30%スクロース溶液で2時間脱水した。さらに，30%スクロース溶液に浸した脳スライスを液体窒素にスクリュー瓶ごと15秒沈め急速に冷凍した。その後，スライスを解凍しTris緩衝生理食塩水 (TBS) で洗浄した。バックグラウンドの染色を減らす為にblocking solution (10%ヤギ正常血清，2%ウシ血清アルブミン) に1時間浸した後，一次抗体 (mouse anti-tyrosinehydroxylase monoclonal antibody, Chemicon International) をimmersion buffer (10%ヤギ正常血清，2%ウシ血清アルブミン，0.5% Triton X in TBS) 内で一晩インキュベートした。次に，TBSで洗浄し，二次抗体 (Alexa Fluor 488 goat anti-mouse IgG, Invitrogen社) を加えて1時間インキュベートした。Biocytinで標識された細胞を染色するためにTBSで洗浄した後に，蛍光標識ストレプトアビジン (Alexa Fluor 594 streptavidin, Invitrogen) を加えて1時間インキュベートした。

**〈2·4〉 細胞形態情報の数値化**　共焦点レーザ走査型顕微鏡 (FV-1000, Olympus社) を用いて，20倍の対物レンズで，0.5-1.0 μm間隔になるように固定脳切片の神経細胞形態の蛍光像を100枚程度撮影した。この際に，二重免疫染色法によって染色したチロシン水酸化酵素 (tyrosinehydroxylase) 陽性細胞をドーパミン作動性細胞とし，それ以外の細胞と区別した。また，樹状突起分岐点を詳細に調べるために，40倍の対物レンズを用いて，0.1 μm

間隔で画像を取り込んだ。その後，画像解析ソフトウエア (Neurolucida, MBF Bioscience) を用いて，細胞形態をトレースした。トレースした点をノードと呼び，そのノード，および，エッジを数値化した。ノード数は，1画像当たり平均して2,000点程度とした。また，数値化したデータを基に，ノードにおいて樹状突起の伸張方向に対する垂直断面積を算出し，断面が円であると仮定した場合の半径を計算した。

### 〈2･5〉 有限要素法によるケーブル方程式の数値計算

通常，円筒形状セグメントの興奮膜の数理モデルは，ケーブル方程式：

$$p(x)\left(c_M\frac{\partial V(x,t)}{\partial t}+\mathcal{J}(x,t)\right)-\frac{\partial}{\partial x}\left(g_A A(x)\frac{\partial V(x,t)}{\partial x}\right)=0$$

$$x\in(0,L),\quad t>0, \qquad \cdots\cdots(3)$$

および，初期条件と両端2つの境界条件から構成される。(3)式では，円筒形の中心軸に沿った長さを $x$，時間を $t$ (ms)，断面積を $A(x)$，円周長を $p(x)$ とする。また，セグメントの芯(コア)のコンダクタンスを $g_A$ (mS/cm)，膜容量を $c_M$ ($\mu$F/cm$^2$) とする。$\mathcal{J}(x,t)$ ($\mu$A/cm$^2$) は，膜を透過するイオンチャネル電流項を表す。セグメントの中心軸に沿ったコア電流は，

$$I(x,t)=-g_A A(x)\frac{\partial V(x,t)}{\partial x} \qquad \cdots\cdots(4)$$

である。本計算における境界条件は，シールドエンドとし，特記しない限り，コア電流は終端点において零であるものとする。Altenberger ら[12]は，有限要素法を1次元ケーブル方程式に適用した膜電位の計算手法を提案した。彼らは，文献(12)で提案手法の精度や誤差を詳細に検討している。以下では，Altenberger らが提案した手法に従って，セグメントに沿って節（ノード）を $n$+1 点設定し，ノード間の $n$ 個の区間を要素（エレメント）とよぶ。また，セグメントを長さ $L$ (cm) として，ノード点の位置を $0=x_0<x_1<\cdots<x_n$ とする。(3)式中の関数 $V, \mathcal{J}, p, A$ を三角形形状（テント）関数を基底関数として，区間 $x\in[0,L]$ において，

$$V(x,t)=\sum_{k=0}^{n}V_k(t)\phi_k(x),\quad A(x,t)=\sum_{k=0}^{n}A_k\phi_k(x),$$
$$\mathcal{J}(x,t)=\sum_{k=0}^{n}\mathcal{J}_k(t)\phi_k(x),\quad P(x,t)=\sum_{k=0}^{n}P_k\phi_k(x), \qquad \cdots\cdots(5)$$

と展開する。したがって，全区間内の任意点 $x$ の電位 $V(x,t)$ を知るためには，電位のサンプル点の有限要素によって，適当に表現する形式を得ればよい。一般に，基底関数列 $\phi_j(x)$ を用いて，関数 $f(x)$ を展開した場合に，真の関数と近似関数との二乗誤差の全区間に渡る積分値：

$$E(f_0,f_1,\ldots,f_n)=\int_0^L\left[f(x)-\sum_{j=0}^{n}f_j\phi_j(x)\right]^2dx \qquad \cdots\cdots(6)$$

を最小とする係数列 $\{f_j\}_{j=0,\ldots,n}$ を求めることができれば，最小2乗誤差の意味で，$f(x)$ の最適な近似関数を得ることができる。実際に，これを実行すれば，(3)式は，

$$P\frac{d\bar{V}}{dt}+P\bar{\mathcal{J}}(t)=A\bar{V} \qquad \cdots\cdots(7)$$

と表記することができる[12]。ただし，ノード点 $x_k$ での電位，断面積，円周長を各々 $v_k$，$a_k$，$p_k$ とし，$\Delta x_k=x_k-x_{k-1}$，$\Delta v_k=v_k-v_{k-1}$，および，$a^k=(a_{k-1}+a_k)/2$ とおくと，行列 $P$ は，対角成分要素を次のベクトル：

$$e_1=\quad c_M[\Delta x_1(3p_0+p_1),\ \Delta x_1(3p_0+p_1)+\Delta x_2(p_1+3p_2),\ldots,$$
$$\Delta x_{n-1}(3p_{n-2}+p_{n-1})+\Delta x_n(p_{n-1}+3p_n),\Delta x_n(p_{n-1}+3p_n)]/12$$

の要素として，その上下の対角成分要素を，共に，

$$e_2=c_M\left[\Delta x_1(p_0+p_1),\ldots,\Delta x_n(p_{n-1}+p_n)\right]/12$$

の要素とする行列である。また，同様に，行列 A は，対角成分要素を次のベクトル：

$$u_1=-g_A[a^1/\Delta x_1,a^1/\Delta x_1+a^2/\Delta x_2,\ \ldots,$$
$$a^{n-1}/\Delta x_{n-1}+a^n/\Delta x_n,a^n/\Delta x_n]$$

の要素として，その上下の対角成分の要素を，共に

$$u_2=g_A\left[a^1/\Delta x_1,\ldots,a^n/\Delta x_n\right]$$

の要素とする。また，$\bar{V}$ はノードにおける電位ベクトルを表し，$\bar{V}=[V(x_0,t),\ldots,V(x_n,t)]'$ である。$\bar{\mathcal{J}}(t)$ は，イオンチャネル電流項を表し，受動的な膜の場合は，リーク電流項のみとなる。本研究では，Altenberger ら[12]の分岐構造を持たない有限要素法表現を拡張した。そして，Y 字形状の分岐構造のある樹状突起の膜電位を計算する方法を新たに導出し，その方法を以下では適用した。ここでは詳細は省略するが，その結果から，分岐構造を持たない場合と同様の行列 $P_Y, A_Y$ が得られる。ただし，Altenberger らが用いた単純なシリンダ形状の行列 $P, A$ とは異なり，対角成分とその上下の成分以外にも零でない要素をもつために，計算には注意が必要である。また，(3)式の偏微分方程式とは異なり，(7)式は常微分方程式であり，時間に関する数値計算手法は一般的な Crank-Nicholson 法を用いた。

## 3. 結　果

### 〈3･1〉 ドーパミン作動性細胞形態の特徴

Fig. 1A に生後15日目の DA 作動性神経細胞の形態を示す。冠状断面の脳切片を作成した為に，線条体等に投射する体軸吻側方向に伸張する軸索は切断されており，Fig. 1A は，主に細胞体と樹状突起であると考えられる。

生後15日齢の11 DA 細胞に対して，(i) 細胞体に接続している主要な樹状突起数は $N_d$=5.45±1.72（平均±標準偏差），(ii) 各樹状突起の分枝に含まれる分岐点数，$B$=2.81±3.07，(iii) 分岐点間のセグメント内における細胞体からの1 μm 当たりの各樹状突起半径の減衰率，$D$=2.05±1.34 %であった。一方，生後3日齢の9 DA 細胞に対して，同様に，(i) $N_d$=4.83±0.87，(ii) $B$=5.17±2.10，(iii) $D$=2.36±1.52%であった。

### 〈3･2〉 Rall の等価シリンダモデル

Fig. 1B は，Fig. 1A と同じ細胞の樹状突起の樹形図を表している。実験によっ

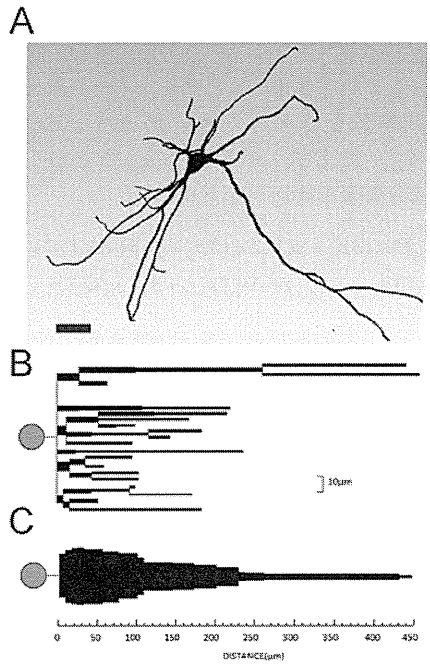


Fig. 1. A, morphology of a dopaminergic neuron from a postnatal day 15 rat. B, schematical representation of dendrites for the cell show in A. C, Rall's equivalent-cylinder representation corresponding one shown in B. A small bar in A indicates 50 μm. Two circles on the left in B and C represent somata.

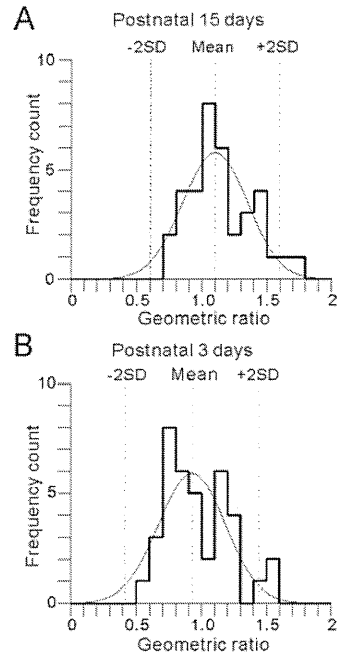


Fig. 2. Histograms for geometric ratio (GR) between a parent branch and daughter branches in dendrites of dopaminergic neurons. A, postnatal 15-day cells. B, postnatal 3-day cells. Dotted lines represent mean and mean ±2SD, respectively. Each curve in the plots shows a normal distribution with the mean and SD.

て得た結果から，(1)式を用いて分岐する樹状突起の半径を等価シリンダモデルに統合させた場合に，この細胞では，前方 1/3 程度が円柱状であり，その後は円錐状の先細り形状になる。Fig. 1C は，その等価ケーブルモデルを表している。Fig. 1C の左端は細胞体を表す。他の DA 細胞でも同様な形状のシリンダとなった。以下では，DA 細胞の形態が単純な Rall の等価シリンダモデルで表現可能であるかを検証する。ここでは，特に，研究方法で述べた（条件 1）を検証する。

**〈3·3〉 樹状突起における Rall の幾何学的比** 生後 15 日目の 7 細胞 36 箇所の分岐点における GR の分布を Fig. 2A に示す。GR の平均は $m$=1.010 であり（Fig. 2A 中の点線中央），その標準偏差は$\sigma$ =0.249 であった。分岐点で Rall の 3/2 乗則が満たされる場合には GR=1 となるために，実際の DA 細胞の多くの分岐点では 3/2 乗則は満たされていない。したがって，(条件 1) が成立しないので，DA 細胞の樹状突起を Rall の等価シリンダで表現して，電気的特性を解析する合理的理由は存在しない。今回の実験で計測したドーパミン細胞の 36 箇所の分岐点では，GR>1 となる分岐点が 23 箇所あり，残りの 13 箇所が GR<1 であった。この結果から，受動的な膜として細胞体から電位が伝播 (backward propagation) する際には，DA 細胞の分岐点での形状は，その数の 60%程度が効率的に伝播しないことが判った。

しかし，反対に，樹状突起末端からシナプス電位が伝播 (forward propagation) する場合には効率が良いことになる。また，細胞間での GR の大きさは，GR=1 を境界として，必ずしも対称に分布しておらず，細胞内でも効率的膜電位伝播となる分岐点とそうではない分岐点が混在することが判った。また，同一細胞の樹状突起の枝においても，GR の値は必ずしも一様ではなかった。

同様に，生後 3 日齢のラットの 10 DA 細胞の 38 箇所の分岐点における GR の分布を Fig. 2B に示す。GR の平均は $m$=0.926 であり（Fig. 2B の点線中央），その標準偏差は $\sigma$ =0.257 であった。10 細胞中の 38 箇所の分岐点で，GR>1 が 15 箇所あり，残りの 23 箇所が GR<1 であった。また，細胞間に大きな偏りは見られなかった。さらに，生後 3 日目と 15 日目の GR 分布の歪度 $s$ は，各々$s$ =0.601 と $s$ =0.510 であり，成長後は GR=1 を中心にして，GR の分布の左右の偏りが小さくなることが判る。

**〈3·4〉 受動的膜モデルシミュレーション** 以降では，生後 15 日齢のラットの DA 細胞の平均的な特徴（分岐数 4，半径の低減率 2.0%）を有する Fig. 3A に概略を示す比較的単純な形状の樹状突起モデルを考える。研究方法で述べた電位の数値計算手法を用いて，Fig. 3B では，Rall の GR 値を分岐点で一定値（GR=0.5, 1.0, および，2.0）に固定し，左端の電位を 40 mV に保持した場合について，定常状態での膜電位を位置の関数として表示している。まず，GR=1 の条件下では，分岐点での膜電位が滑らかに変化する。

一方，GR=0.5，あるいは，GR=2.0 の条件では，分岐点で

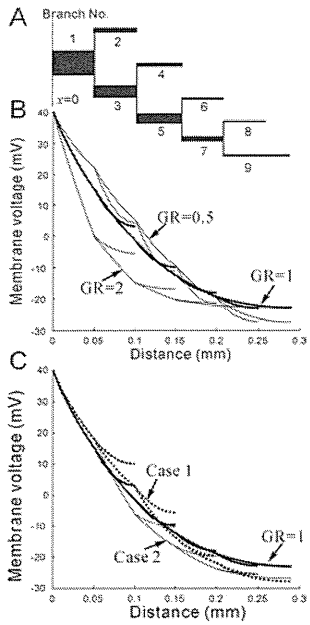


Fig. 3. A, schematic representation of a simple dendrite. B, relationship between membrane voltage vs. distance from soma for three cases of GR=0.5, 1.0, and 2.0. C, a similar plot shown in B. Parameters of dendrites in Case 1 and 2 were taken from experimental data.

膜電位変化の傾きが変化し，曲線の一次導関数は不連続であることが判る。さらに，GR=2.0 の条件では，電位曲線は GR=1.0 の下側にあり，GR=0.5 では殆どが GR=1.0 の曲線の上側に電位がある。このことから，GR がより大きくなると，電位が伝播する際に，その減少率が大きくなることが判る。既に述べたように，Rall はこの状況を伝播効率が悪い場合とよんだ。

次に，2 つの DA 細胞の樹状突起から得た実際の計測データ例（Case 1 and Case 2）を基に GR，および，半径を決定し，Fig. 3B と同様な枝の長さやパラメータ等の条件で膜電位の空間的変化を表した図を Fig. 3C に示す。また，同時に，Fig. 3B の GR=1 の場合を重ね書きした。計測値では，同じ樹状突起の枝であっても，GR が 1 の前後の値を不規則に取る為に，GR=1 の曲線を上から下に，あるいは，その逆方法に横切る。しかし，樹状突起全体の電位変化としては，GR=1 の曲線を覆うようになり，極端に電位減少が見られることはない。さらに，同一の樹状突起の枝に関して，分岐点が全て GR>1,もしくは，GR<1 を満たす場合がみられなかったことから，受動的膜特性として，ある特定の樹状突起の枝が特異的に効率の良い（あるいは，悪い）ものに特化しているのではないことが推測される。また，上記は細胞間にも同様のことが言える。

## 4. 議　論

〈4･1〉　スライスの作成と細胞膜電位記録　　本研究では，ラット黒質緻密部の DA 細胞の形態を詳細に計測した。その結果，細胞体から樹状突起の先端部までの距離は，500-900 μm に及び，DA 細胞は，広範囲に渡ってシナプス入力を時空間的に統合できる可能性を示唆している。生後 15 日目の DA 細胞では，平均して，細胞体から 5-6 本の樹状突起が伸び，2-3 回程度の枝分かれが生じていることが判った。一方，生後 3 日目の DA 細胞では，樹状突起の枝分かれの数は 5-6 回程度であり，生後 15 日までにそれらの枝が半分程度に刈り込まれることを示している。

一般に，神経細胞では，シナプス入力が細胞膜の電位を上昇させ，樹状突起から細胞体，軸索にその電位が伝達され，活動電位が軸索基部で発生する。この現象は，forward propagation とよばれる。一方，軸索の一部領域にある活動電位発生部位から，活動電位が樹状突起先端部に伝播する現象は，back propagation とよばれる。現在，活動電位は，神経情報の担い手であると考えられていることから，この符号化過程を理解することは神経科学の中心的な課題である。特に，単一細胞での活動電位の発生の時空間的シナプス統合過程に関しては，多くの先行研究がある[16]。

Rall は，その先駆的な研究によって，神経細胞の膜電位が時間発展する規則をケーブル方程式などの単純な偏微分方程式に置き換え，3 次元形態をもつ神経細胞を簡略化する方法を提案した。特に，細胞形態をシリンダ状の形状に分割し，その集合体として扱うことによって，膜電位の伝播効率をシリンダの半径の関係と結びつけた。本研究では，この枠組みに従い，実測データに基づき，DA 細胞形態を受動的膜と仮定した場合の伝達効率を理解しようと試みた。その結果，DA 細胞の多くの分岐点では，Rall の 3/2 乗則は厳密には満たされておらず，Rall の言う意味での膜電位伝播は，細胞間，および，細胞内でも多様であることが窺える。この事実は，脊髄の運動ニューロンが Rall の 3/2 乗則をほぼ満たしているのとは対照的である。しかし，今回の計測では，Rall の定義した GR 値は，多くの分岐点で 0.8-1.4 の範囲に含まれており，極端に大きく 1 から外れていなかった。また，発達時期に従って，GR のヒストグラムが GR=1 を中心とした左右対称な分布に変化することから，ドーパミン細胞集合全体では，Rall の 3/2 乗則に従う方向に変化すると考えられる。さらに，今回の実験データは 300 μm 厚の脳スライスという限られた組織空間のサンプル値であり，実験の制約条件を差し引いて評価する必要もある。

同じ樹状突起内の枝に Rall の意味での伝播効率が良い分岐点と悪い分岐点が混在していることの機能的な意味は不明である。推測としては，一つの樹状突起の枝の入力信号を特異的に強調するのではなく，全体の入力をバランスさせ，平均化する機能をもつのかも知れない。そして，極端に Rall の 3/2 乗則から外れる枝は，発達の段階が進むに従って，刈り込まれる可能性もある。

本研究では，イオンチャネル電流を含む能動的膜について考慮しなかった。しかし，近年の研究に拠ると，海馬や小脳の神経細胞と異なり，DA 細胞は活動電位波形を維持し

たまま樹状突起の先端部付近まで，back propagation を伝播させることができることが明らかになっており[17]，能動性の考慮は次の重要課題である。また，DA 細胞では，軸索以外にも樹状突起で活動電位を発生させることが知られている。したがって，複数の活動電位発生部位から発生した電位が様々な方向に伝播し，神経伝達物質ドーパミンを放出しながら自己抑制することになり，そこではさらに複雑な情報処理を行っている可能性がある。

本研究では，Altenberger ら[12]の方法に従って，従来のコンパートメントモデルとは異なる有限要素法を用いた神経細胞形態の計算機上への実装方法を述べた。本研究では，特に，Altenberger らの方法を拡張して，Y 字形状の分岐点を有する樹状突起形状に対し新たに応用する方法を簡単に述べた。1 次元のコンパートメントモデルは，計算神経科学の分野で汎用的に利用されているが，空間的に分布する膜電位の変動を見る際に，連続体モデルとの乖離が生じることが指摘されている[18][19]。特に，Y 字型コンパートメント自体を一つの「パーツ」として考慮することができない為に，どの様に小さくコンパートメントを分割しても，分岐点で位置に関するいくつかの変数の一次導関数の連続性が失われる（Fig. 3 参照）。この点は，1 次元のコンパートメントの「モデル固有」の問題点であり，3 次元連続体モデルでは，変数の高次導関数も滑らかに変化する点は注意を要する。したがって，近年多く用いられている汎用神経シミュレータの結果が実際の細胞でも妥当であるとは必ずしも言えない。今回用いた方法は 3 次元に容易に拡張が可能であるが，基本的には，1 次元のコンパートメントモデルと類似の方法であり，同様の誤った解釈をしている可能性は否定できない。これらを検証するためには，樹状突起の立体形状を詳細に考慮し，2 次元，および，3 次元モデルへの拡張によって，本研究の問題点を再検討する必要があり，今後の課題としたい

## 5. 結　論

本研究では，中脳黒質の DA 細胞の発達に伴う変化を，その特徴と機能の両面から理解することを目指した。本稿では，特に，中脳黒質 DA 細胞の生後発達の初期ステージにおける形態的特徴を対象とした。実測データに基づき，DA 細胞形態を受動的膜と仮定した下で，伝達効率の観点から形態変化の特徴を理解しようと試みた。その結果，DA 細胞の多くの分岐点では，Rall の 3/2 乗則は厳密には満たされておらず，Rall の言う意味での膜電位伝播は，細胞間，および，細胞内でも多様であることが明らかになった。

**謝　辞**

本研究の一部は，科学技術振興機構さきがけ研究「生命現象の革新モデルと展開」，および，科研費基盤研究（B），新学術領域「伝達創成機構」および，萌芽研究の助成によって行われた。

（平成 22 年 4 月 12 日受付，平成 22 年 6 月 21 日再受付）

## 文　献

(1) M. B. Carpenter : "Core Text of Neuroanatomy", 4th Ed., Williams & Wilkins, Baltimore, Chap.11 (1991)
(2) B. Liss and J. Roeper : "Individual dopamine midbrain neurons: Functional diversity and flexibility in health and disease", Brain Res. Rev., Vol.58, No.2, pp.314-321 (2007)
(3) W. Schultz : "Predictive reward signal of dopamine neurons", J. Neurophysiol., Vol.80, No.1, pp.1-27 (1998)
(4) M. F. Beal : "Excitotoxicity and nitric oxide in Parkinson's disease pathogenesis", Ann. Neurol., Vol.44, No.3, pp.S110-114 (1998)
(5) C. S. Chan, J. N. Guzman, E. Ilijic, J. N. Mercer, C. Rick, T. Tkatch, G. E. Meredith, and D. J. Surmeier : "'Rejuvenation' protects neurons in mouse models of Parkinson's disease", Nature, Vol.447, No.7148, pp.1081-1086 (2007)
(6) A. Cheramy, V. Leviel, and J. Glowinski : "Dendritic release of dopamine in the substantia nigra", Nature, Vol.289, No.5798, pp.537-543 (1981)
(7) C. J. Wilson and J. C. Callaway : "Coupled oscillator model of the dopaminergic neuron of the substantia nigra", J. Neurophysiol., Vol.83, No.5, pp.3084-3100 (2000)
(8) S. Kuznetsov, N. J. Kopell, and C. J. Wilson : "Transient high-frequency firing in a coupled-oscillator model of the mesencephalic dopaminergic neuron", J. Neurophysiol., Vol.95, No.2, pp.932-947 (2006)
(9) W. Rall : "Branching dendritic trees and motoneuron membrane resistivity", Exptl. Neurol., Vol.1, No.1, pp.491-527 (1959)
(10) W. Rall : "Theoretical significance of dendritic trees for neuronal input-output relations", in Neural Theory and Modeling, ed. R. F. Reiss, pp.73-97, Stanford University Press, Palo Alto, CA (1964)
(11) W. Rall : "Membrane potential transients and membrane time constant of motoneurons", Exptl. Neurol., Vol.2, No.5, pp.503-532 (1960)
(12) R. Altenberger, K. A. Lindsay, J. M. Ogden, and J. R. Rosenberg : "The interaction between membrane kinetics and membrane geometry in the transmission of action potentials in non-uniform excitable fibres: a finite element approach", J. Neurosci. Methods, Vol.112, No.2, pp.101-117 (2001)
(13) W. Rall : "Core conductor theory and cable properties of neurons", in The Nervous System, Vol.I : Cellular Biology of Neurons, Part I, ed. E. R. Kandel, Bethesda, American Physiological Society, pp.175-187 (1977)
(14) J. W. Fleshman, I. Segev, and R. E. Burke : "Electrotonic architecture of type-identified alpha-motoneurons in the cat spinal cord", J. Neurophysiol., Vol.60, No.1, pp.60-85 (1988)
(15) W. Rall : "Change of action potential shape and velocity for changing core conductor geometry", Biophys. J., Vol.14, No.10, pp.731-757 (1974)
(16) N. Spruston, G. Stuart, and M. Hausser : "Dendritic integration, in Dendrites", Eds. Stuart G. Spruston N. Hausser M. Oxford University Press, Oxford, Chap.14 (2008)
(17) P. Vitter, A. Roth, and M. Hausser : "Propagation of action potentials in dendrites depends on dendritic morphology", J. Neurophysiol., Vol.85, No.2, pp.926-937 (2001)
(18) A. E. Lindsay, K. A. Lindsay, and J. R. Rosenberg : "New concepts in compartment modeling", Comput. Visual. Sci., Vol.10, pp.79-98 (2007)
(19) K. A. Lindsay, J. R. Rosenberg, and G. Tucker : "From Maxwell's equations to the cable equation and beyond", Prog. Biophys. Mol. Biol., Vol.85, No.1, pp.71-116 (2004)

**舘　野　　高**

（正員）　1968 年 8 月 7 日生。1992 年 3 月大阪大学基礎工学部生物工学科卒業。1994 年 3 月同大学大学院基礎工学研究科博士前期課程修了（生物工学）。1994 年 4 月 NTT 基礎研究所勤務。1999 年 4 月大阪大学大学院基礎工学研究科助手。2002 年から 2004 年 Cambridge 大学客員研究員，並びに，日本学術振興会海外特別研究員兼務。2007 年 4 月大阪大学大学院基礎工学研究科准教授。2007 年 10 月から科学技術振興機構さきがけ研究員兼務。現在，神経細胞の電気生理学に関する研究，および，微細加工技術を応用した人工感覚器開発に従事。

# Synchronization of Firing in Cortical Fast-Spiking Interneurons at Gamma Frequencies: A Phase-Resetting Analysis

**Nathan W. Gouwens[1,2☯], Hugo Zeberg[1,3☯], Kunichika Tsumoto[4,5], Takashi Tateno[6,7], Kazuyuki Aihara[4,5], Hugh P. C. Robinson[1]***

**1** Department of Physiology, Development and Neuroscience, University of Cambridge, Cambridge, United Kingdom, **2** Department of Neurobiology, Harvard Medical School, Boston, Massachusetts, United States of America, **3** Nobel Institute for Neurophysiology, Department of Neuroscience, Karolinska Institutet, Stockholm, Sweden, **4** Aihara Complexity Modelling Project, ERATO, Japan Science and Technology Agency, Tokyo, Japan, **5** Institute of Industrial Science, The University of Tokyo, Tokyo, Japan, **6** Graduate School of Engineering Science, Osaka University, Osaka, Japan, **7** PRESTO, Japan Science and Technology Agency, Saitama, Japan

## Abstract

Fast-spiking (FS) cells in the neocortex are interconnected both by inhibitory chemical synapses and by electrical synapses, or gap-junctions. Synchronized firing of FS neurons is important in the generation of gamma oscillations, at frequencies between 30 and 80 Hz. To understand how these synaptic interactions control synchronization, artificial synaptic conductances were injected in FS cells, and the synaptic phase-resetting function (SPRF), describing how the compound synaptic input perturbs the phase of gamma-frequency spiking as a function of the phase at which it is applied, was measured. GABAergic and gap junctional conductances made distinct contributions to the SPRF, which had a surprisingly simple piecewise linear form, with a sharp midcycle break between phase delay and advance. Analysis of the SPRF showed how the intrinsic biophysical properties of FS neurons and their interconnections allow entrainment of firing over a wide gamma frequency band, whose upper and lower frequency limits are controlled by electrical synapses and GABAergic inhibition respectively.

**Citation:** Gouwens NW, Zeberg H, Tsumoto K, Tateno T, Aihara K, et al. (2010) Synchronization of Firing in Cortical Fast-Spiking Interneurons at Gamma Frequencies: A Phase-Resetting Analysis. PLoS Comput Biol 6(9): e1000951. doi:10.1371/journal.pcbi.1000951

**Editor:** Lyle J. Graham, Université Paris Descartes, Centre National de la Recherche Scientifique, France

**Received** March 21, 2010; **Accepted** September 3, 2010; **Published** September 30, 2010



**Funding:** Supported by grants from the BBSRC and EC (HPCR), Daiwa Foundation (HPCR and KA), MEXT Grant-in-Aid for Scientific Research on Priority Areas No. 17022012 and FIRST, Aihara Innovative Mathematical Modelling Project, the Japan Society for the Promotion of Science (JSPS)(KA), and a Churchill Foundation Scholarship (NWG). The funders had no role in study design, data collection and analysis, decision to publish, or preparation of the manuscript.

**Competing Interests:** The authors have declared that no competing interests exist.

* E-mail: hpcr@cam.ac.uk

☯ These authors contributed equally to this work.

## Introduction

Rhythmic oscillations of concerted electrical activity can occur in the neocortex and hippocampus at gamma frequencies (30–80 Hz), and are thought to be associated with a variety of cognitive tasks including sensory processing, motor control, and feature binding [1,2]. A striking feature of gamma oscillations is their ability to be generated locally in the neocortex. Local gamma oscillations can be produced by pharmacological [3,4], electrical [5] or optogenetic [6] stimulation. *In vivo*, synchronous gamma oscillations may be highly localized or widely distributed, even between hemispheres, with or without phase lags between different areas and layers [1]. It appears, therefore, that local neocortical circuits have an intrinsic capability for generating gamma oscillations, while sensory inputs and connections from other brain regions may shape the complex spatial patterns of oscillatory interaction.

Synchronized firing of cortical inhibitory interneurons has been implicated in the production of these rhythms in many experimental and modeling studies. During spontaneous network activity of the neocortex *in vivo*, the power of intracellular voltage fluctuations at frequencies higher than 10 Hz is dominated by inhibitory postsynaptic potentials, which are correlated with the extracellular gamma rhythm, and which synchronously inhibit nearby pyramidal cells [7]. A recent study using conductance injection in neocortical pyramidal cells indicated that gamma-frequency-modulation of firing is almost completely determined by their inhibitory input [8]. In the hippocampus and cortex, models of interneuron activity suggest that network oscillations depend on mutually inhibitory synaptic conductances [9,10,11].

Fast-spiking (FS) inhibitory interneurons are coupled by electrical synapses in addition to mutual and autaptic inhibitory synapses [12,13,14,15]. Electrical synapses alone [12,13] or in combination with GABAergic synapses [14] can produce synchronous firing in pairs of these interneurons *in vitro*. In addition, the biophysical properties of FS neurons appear to be ideally suited to generating gamma rhythms: they have a hard ("type 2") onset of regular firing at about 30 Hz [16], which means that they can be easily entrained at this frequency. They also show a strong intrinsic drive for spike generation at gamma frequencies when stimulated with broadbrand conductance noise [17]. Recently, selective optical stimulation of FS interneurons, but not of pyramidal neurons, was shown to cause gamma oscillations [6]. Electrical synapses amongst mutually inhibitory interneurons have

## Author Summary

Oscillations of the electrical field in the brain at 30–80 Hz (gamma oscillations) reflect coordinated firing of neurons during cognitive, sensory, and motor activity, and are thought to be a key phenomenon in the organization of neural processing in the cortex. Synchronous firing of a particular type of neuron, the inhibitory fast-spiking (FS) cell, imposes the gamma rhythm on other cells in the network. FS cells are highly interconnected by both gap junctions and chemical inhibition. In this study, we probed FS cells with a synthetic conductance stimulus which mimics the electrical effect of these complex connections in a controlled way, and directly measured how the timing of their firing should be affected by nearby FS neighbours. We were able to fit a mathematically simple but accurate model to these measurements, the "synaptic phase-resetting function", which predicts how FS neurons synchronize at different frequencies, noise levels, and synaptic connection strengths. This model gives us deeper insight into how the FS cells synchronize so effectively at gamma oscillations, and will be a building-block in large-scale simulations of the FS cell network aimed at understanding the onset and stability of patterns of gamma oscillation in the cortex.


been found to increase the precision of synchrony in simulation studies [18,19,20]. However, the relative roles of chemical inhibition and gap-junctional coupling in shaping synchronous oscillations in the cortex are still unclear.

The theory of synchronization of coupled oscillators uses the concept of phase dynamics to evaluate the stability of the relative phase of coupled oscillators in time [21,22]. The key to this approach is to determine the effect of a very small perturbing input on the phase of oscillation ("phase resetting"), as a function of the point in the oscillation cycle at which it occurs. This is most often used, under the assumptions of weak coupling and linear summation of phase shifts, to account for how the relative phase of presynaptic and postsynaptic cells evolves from cycle to cycle.

However, as described above, FS cells in the cortex are actually coupled quite strongly to other FS neighbours, with large postsynaptic conductance changes caused by each presynaptic action potential. Here, we have used synthetic conductance injection, or dynamic clamp, to directly measure the phase-resetting response to conductance inputs mimicking the effects of presynaptic action potentials, while systematically varying the relative strengths of electrical and GABAergic inhibitory conductances. The compound synaptic connections between FS neurons, together with the intrinsic spike-generating properties of FS neurons, give rise to a distinctively-shaped phase-resetting relationship, or "synaptic phase-resetting function", which ensures rapid and precise synchronization over a large gamma-frequency range.

## Results

### Conductance injection reproducing synaptic input

FS cells in rat somatosensory cortical slices were identified by their morphology, action potential shape and characteristic firing pattern in response to depolarizing current injection [12,13,23,24]. FS cells fired high frequency, nonadapting trains of action potentials during depolarizing current steps, occasionally interrupted by pauses with subthreshold oscillations, particularly around threshold [16] (see Methods). We used conductance injection/dynamic clamp [25,26] to reproduce the effects of electrical and chemical synapses (Fig. 1, see Methods). In FS cells, both gap junctions and GABAergic synapses from neighboring cells are located perisomatically [14], so that point conductance injection at the soma should reasonably reproduce the electrical effects of synaptic inputs. Gap junctions were implemented as a static conductance between the recorded cell and a "voltage-clamped" trajectory of "presynaptic" membrane potential. This "voltage-source" approximation, importantly, allowed us to characterize a functional mapping between the presynaptic spike time and the influence on postsynaptic membrane potential, without considering any reverse effect of gap-junctional current on the presynaptic cell. This is valid as long as the presynaptic cell is considered to be much more strongly controlled by its other inputs, as when it is already part of a synchronous assembly (see Discussion). It is estimated that each FS cell is gap-junction coupled, directly or indirectly, with a measurable coupling, to between 20 and 50 other FS neurons [27], so that if the presynaptic cell is quite strongly-driven by a major proportion of these inputs, then the effect of any one can be neglected. At rest, this gap-junctional input produced a small postsynaptic spikelet (Fig. 1a, left), very similar in size and shape to those observed with natural electrotonic coupling [12,13]. We also measured coupling coefficients (the ratio of postsynaptic to presynaptic potential change) for gap-junctional type conductance. These were similar to physiological values, and larger for step inputs (0.05–0.22) than for spike inputs (0.01–0.05), owing to low-pass filtering by the combined effects of gap junctional conductance and membrane resistance and capacitance [28].

Many pairs of FS cells are connected by both GABAergic ($GABA_A$, chloride conductance) and electrical synapses [12,13,14]. We simulated GABAergic synaptic input using conductance injection (Fig. 1a, middle). The GABA reversal potential ($E_{GABA}$) was set to −55 mV, based on gramicidin-perforated patch measurements in this cell type [10,29], considerably more depolarized than in pyramidal neurons [30]. Thus, inhibition is shunting in the range of membrane potentials between spikes during repetitive firing (Fig. 1b). Starting from the resting potential, the "IPSP" is a small depolarisation lasting about 40 ms, again very similar to natural IPSPs in these cells. At the resting potential, a stimulus with both electrical and GABAergic components produces a biphasic depolarizing response (Fig. 1a, right) with the gap-junctional potential visible just before the larger GABAergic potential. Unlike the gap-junctional spikelet, though, the amplitude of the GABAergic potential can change sign in the subthreshold, interspike range of membrane potentials, reversing around $E_{GABA}$ [12].

### Perturbing spike timing

To determine how this compound synaptic input shifts the timing of periodic firing in an FS cell, we applied conductance inputs during periodic firing elicited by a maintained excitatory stimulus, a step of excitatory conductance reversing at 0 mV. An example response to a compound "synaptic" perturbation is shown in Fig. 1b. In phase-resetting analysis of synchronization, the state of the neuron is characterized by a single quantity, the phase angle, $\phi(t)$, which – in the absence of any perturbations - increases linearly with time, and which is reset to zero whenever it reaches $2\pi$, corresponding to the occurrence of a spike [21]. The variability of interspike intervals can be represented by adding additional noise, due to stochastic gating of ion channels and other intracellular sources of variability, to the rate of change of $\phi(t)$. To measure the phase *resetting*, or shift in the phase, produced by synaptic-like conductance inputs, we applied isolated single inputs during long trains of periodic firing. Fig. 1c shows the relationship between the time $t_p$ at which an input (in this case a compound

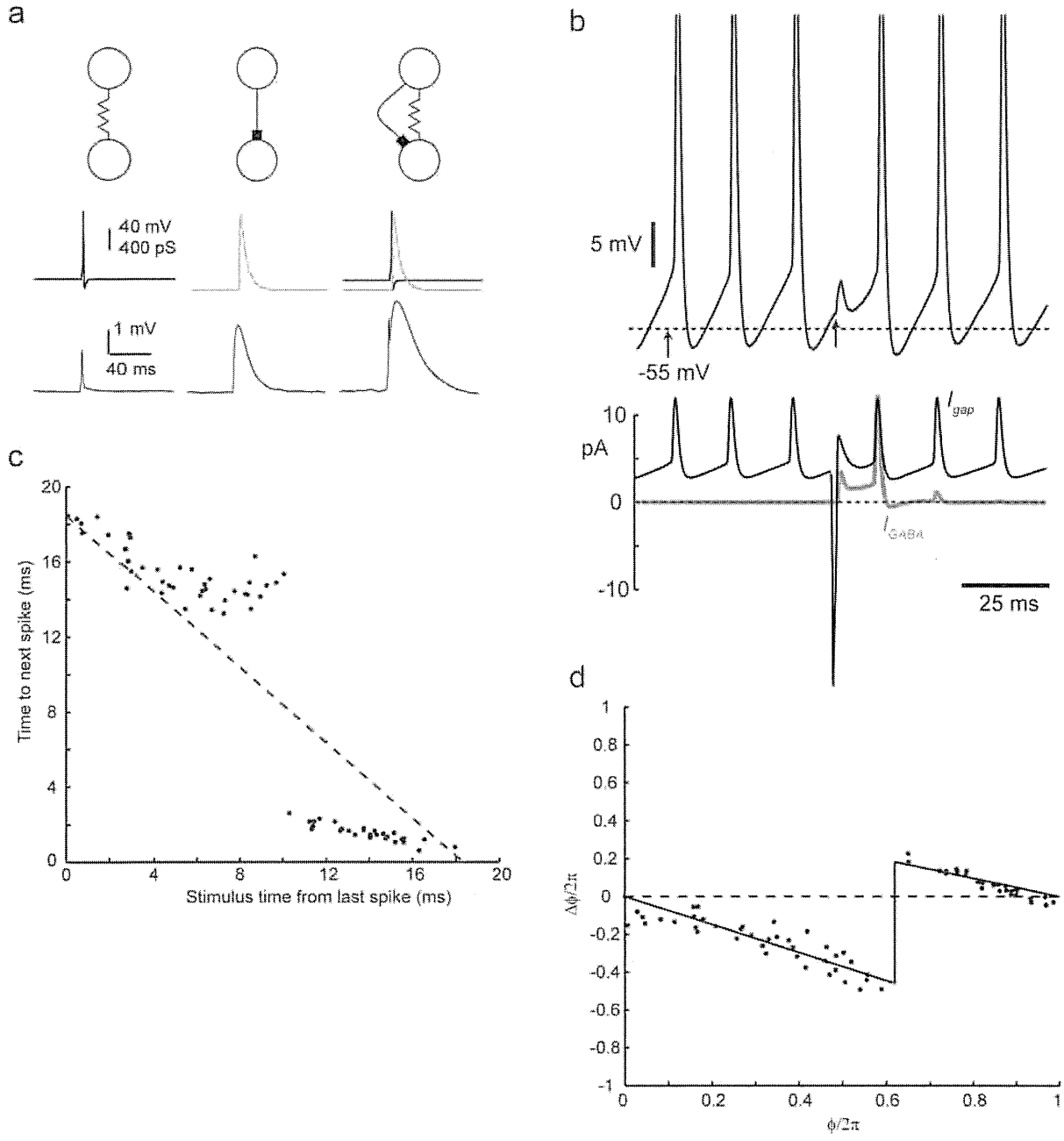


**Figure 1. Synaptic connections between FS cells simulated by conductance injection.** a) *Left*, an electrical synapse (*top*), simulated by a time-varying $E_{rev}$ signal (*middle*), and a constant conductance of 750 pS, produces a spikelet in the recorded neuron (*bottom*). *Center*, a GABAergic synapse (*top*). A transient of conductance reversing at −55 mV mimics a $GABA_A$ synaptic input (*middle*), producing a small depolarization from rest (*bottom*). *Right*, a compound electrical/GABAergic connection (top). Combined input from both types of conductances (*middle*) produced a response with a sharp, electrical synaptic component followed by a longer-lasting IPSP (*bottom*). Each panel is recorded from a different cell. b) expanded view of the membrane potential trajectory (top, spike peaks truncated) and injected currents (bottom, gap-junctional current in black, current through GABAergic conductance in gray, outward current is represented upwards) during application of a single compound conductance perturbation ($g_e$=0.2 nS, $g_i$=1.4 nS) starting at the time indicated by an arrow, in this case inducing a delay in the subsequent spike time. c) Relationship between time at which input is applied and the time to next spike and d) corresponding phase-resetting relationship, or synaptic phase-resetting function.
doi:10.1371/journal.pcbi.1000951.g001

gap/GABA input) is applied, relative to the time of the preceding spike, and the time until the next spike occurs ($t_n$). This clearly deviates from the line of slope −1 (dotted line) expected in the absence of any input, and has two approximately linear regions separated by a sharp transition. Note the characteristic progressive decrease in the variability of this relationship, as $t_p$ increases – this is because the earlier the input arrives, the more time is left for integrating the effects of noise before the next spike.

## The synaptic phase-resetting function and the effect of varying electrical and inhibitory conductances

From this relationship, we can estimate the phase at the moment that each input is applied, and the amount of phase resetting $\Delta\phi$ produced by the input (see Methods), as shown in Fig. 1d, in which $\Delta\phi$ is plotted as a function of $\phi$. This relationship - the total phase-resetting effect of a synaptic input as a function of the phase at which it arrives – we will refer to as a synaptic phase-resetting function (SPRF), to distinguish it from a classical phase response or phase-resetting curve, which normally describes responses to very small, brief inputs, whose effects can be considered to sum linearly. We examined how the parameters of the synaptic input determine the shape of the SPRF, by varying the magnitude of gap-junctional and GABAergic conductance, applied individually or together (Fig. 2a–f). These components vary physiologically, since FS cells' interconnections can be purely GABAergic (one-way or reciprocal), purely gap-junctional or both [12,13,14]. In addition, there is a wide range of electrical synaptic strengths [28].

Purely GABA input produced a phase delay early in the cycle, which increased during the cycle until an abrupt critical point, beyond which it had no effect (Fig. 2a). Introducing a small (250 pS) gap junction, caused a linear region of phase advance (Fig. 2b), as in Fig. 1d, which had an abrupt onset at a phase of about $1.2\pi$. A sharp transition marks the boundary between this region and the first, phase delay part of the phase cycle. The slope of the phase advance region became more negative, and the boundary between the regions, designated the critical phase $\phi_c$, shifted earlier in the cycle, as gap junctional conductance increased (Fig. 2c, d, e). With no GABAergic input, a phase advance region produced by gap junctional input is seen in isolation (Fig. 2f).

Thus, GABAergic input retards, and gap-junctional input advances the phase of firing. For the compound gap/GABA input, the early region of phase delay has a slope determined by the amplitude of inhibition, $g_i$ (see Methods), and switches abruptly, midcycle, to a region of decreasing phase advance, whose slope is determined by $g_e$, with no detectable sign of cancellation of the two regions in midcycle. The only clear interaction between the electrical and GABAergic components was that a larger gap junctional conductance shifted $\phi_c$ to earlier in the cycle.

To quantify the goodness of fit of the piecewise linear SPRF, we performed a chi-square test of 130 phase response curves (in total 6111 data points, 10 cells). For each SPRF, variance of phase was estimated from an unperturbed spike train within the same experiment (median $\sigma^2 = 0.021$ (rad/$2\pi$)$^2$. 111 of 130 SPRFs contained no significant difference between the model fit and experimental result ($p<0.05$). The average reduced chi-square value was 0.80, meaning that the overall fit of the model is extremely good, given the measured degree of variance in the phase. On the whole, the relatively simple piecewise linear model performs remarkably well.

The dependencies of the slopes and breakpoint on the strengths of $g_i$ and $g_e$ were also fitted by linear relationships (Figure 3). The negative slope of the region of phase delay was proportional to inhibition ($\alpha = ag_i$, Fig. 3b), the negative slope of the phase advance region was proportional to excitation ($\beta = bg_e$, Fig. 3a), while $\phi_c$ was weakly sensitive to $g_e$ ($\phi_c = c - dg_e$, Fig. 3c). Average values of $a$ and $b$ of this piecewise linear model for the SPRF were $a = 0.16$/nS (n = 7 cells, 3 cells providing insufficient data for analyzing this dependency), b = 0.69/nS (n = 10 cells). $c$ and $d$ were more variable from cell to cell, and the pooled data in fact showed little overall dependence on $g_e$ (not shown). Nevertheless (e.g. Fig. 3c), the weak relationship is clear within individual cells.

## Entrainment by synaptic input

Having established that conductances resembling the synaptic input of neighboring FS cells can consistently modify spike timing, we next tested the ability of FS cells to synchronize to, or to be entrained by this input. To visualize the time course of entrainment, we examined responses stroboscopically [22], sampling the phase of the FS cell at the times of periodic stimuli. Figure 4 shows such an experiment. Before the conductance pulses are switched on (*open circles*), the phase changes in a "sawtooth" pattern, reflecting detuning - the continuously growing phase difference between two oscillators of different frequencies. After the conductance transients begin (Fig. 4, *filled circles*), the phase quickly converges on a fixed value relative to the stimulus, at about $0.6\pi$ (dashed line), which matched the expected equilibrium phase difference from solving Equation 2 with parameters for this cell. Thus the FS cell becomes phase-locked and frequency-locked to the stimulus train, with spikes occurring around $0.6\pi$ before, or equivalently $1.4\pi$ after each stimulus. After the end of the stimulation train, the phase reverts to the drifting detuned state.

The piecewise linear SPRF could also account for the frequency band over which synchronization was possible. Fig. 5 shows an experiment in which an FS neuron firing at a steady frequency $F$ was stimulated repeatedly with a periodic synaptic conductance input at frequency $f$, and an index of the synchrony of the cell with the input ($S$, varying between 0 and 1, see Methods) was measured over a range of frequencies. As seen in Fig. 5a, this changes from a low level when $f$ is very different from $F$, to a high value approaching 1, when $f \approx F$. Because of the effects of noise in the neuron, there is no absolute phase locking ($S<1$), and the change in synchrony with input frequency does not have abrupt boundaries, but falls away continuously as the difference between $f$ and $F$ grows. It is clear that the central region of high synchrony lies below the unperturbed or natural firing frequency $F$ when only inhibition is applied (Fig. 5b), above $F$ when only gap-junctional conductance is applied (Fig. 5c), or both above and below $F$ when a compound input is applied (Fig 5a). This observation was duplicated by the piecewise linear model of the SPRF, analysis of which (see Methods) predicted the 1:1 synchronized frequency bands shown in gray, for the deterministic (noise-free) case – in this neuron, these boundaries corresponds to a synchrony of about 0.7. The synchronized frequency band is much narrower for either gap-junctional stimulation alone (Fig. 5b) or GABAergic inhibition alone (Fig. 5b). Iterations of the noisy stroboscopic map derived from the fitted SPRF (Eq. 2) showed that it could also reproduce the distribution of $S$ adequately (black curves in Fig. 5a–c). Thus the piecewise linear model of the SPRF appears to account very well, both for the frequency range and degree of synchronization in noise.

## Frequency bands of deterministic and stochastic synchronization

We next used the SPRF to predict the frequency ranges of entrainment for different strengths of inhibition and electrical coupling (Fig. 6), by analyzing the bifurcations at the onset of synchrony in the stroboscopic map of the phase, i.e. the map of the phase of the postsynaptic cell at successive presynaptic spike times in a regular train (see Methods, equation 2). For the deterministic (zero noise) case, 1:1 entrainment corresponded to a stable fixed point of the map, labelled $\phi*$ in the example shown in Fig. 6a. As the amount of detuning (difference between $f$ and $F$) varies, the map shifts vertically, so that at certain stimulus frequencies, the fixed point

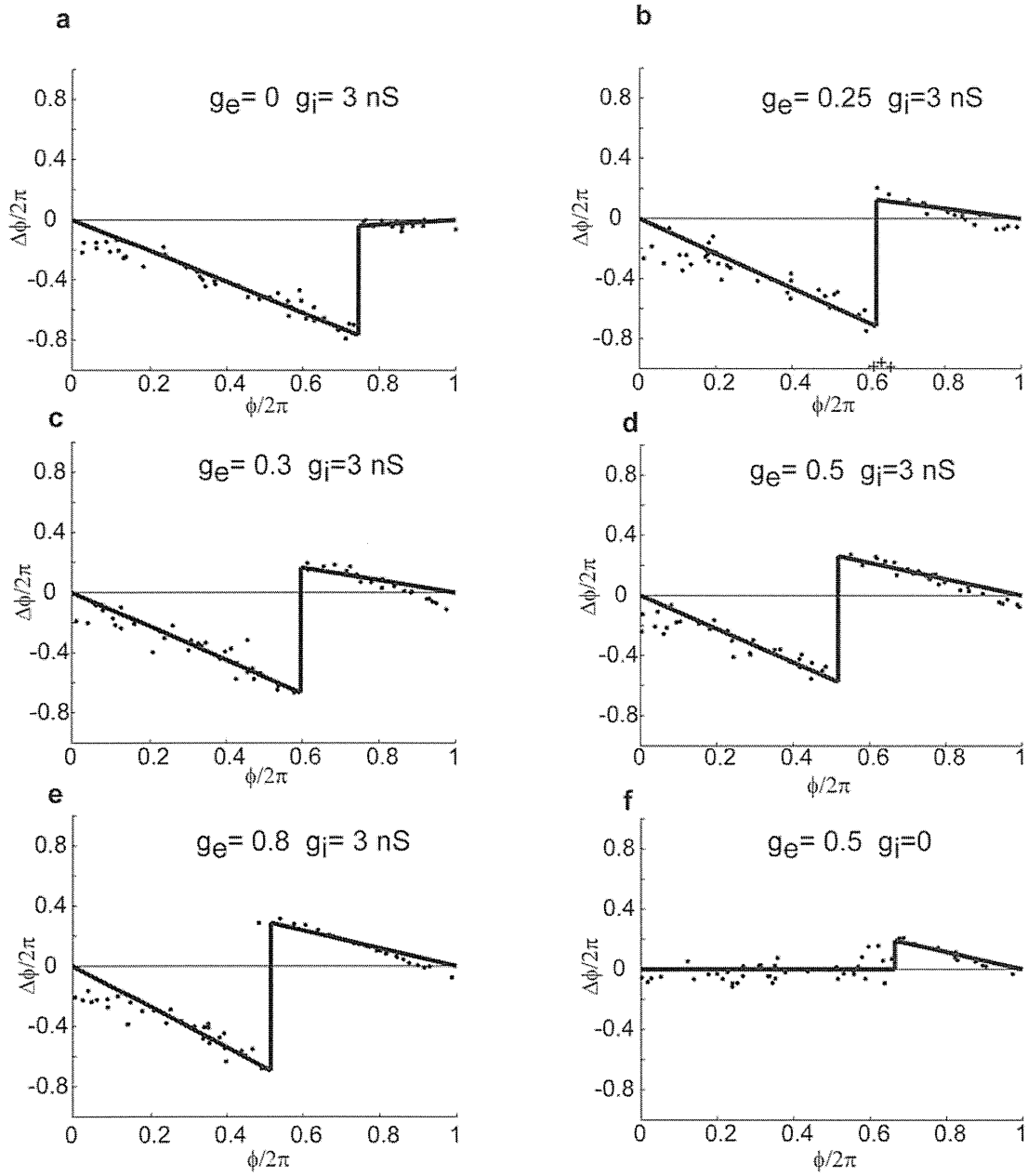


**Figure 2. SPRFs in one cell for different strengths of gap-junctional and inhibitory conductance.** a) inhibition only. Phase delay increases linearly as the phase of onset of the synaptic perturbation increases, before an abrupt loss of sensitivity late in the cycle. b) As gap-junctional conductance is introduced, phase delay switches to a region of linear phase advance late in the cycle "+" symbols indicate outliers excluded from the piecewise linear fit using Grubbs' test, as described in the Methods. c), d), e). As gap-junctional conductance is increased, the slope of the phase advance region becomes larger, and the point of switching is shifted progressively earlier in the cycle. f. switching off inhibition completely leaves only the late phase advance (compare to (d)).
doi:10.1371/journal.pcbi.1000951.g002

disappears (at a "corner-collision" bifurcation [31]). Thus, it is possible to plot the regions in which there is synchronization in the $g_e$,$f$ plane (Fig 6b) or the $g_i$,$f$ plane (Fig. 6c,d). These form Arnol'd tongues [22] in which the frequency range of entrainment shrinks as the synaptic strength is reduced.

This analysis shows a number of effects which are relevant to the physiological function of FS neurons. Increasing $g_e$ strongly increased the upper frequency limit of entrainment and weakly increased the lower limit (Figs. 6b). When $g_i = 0$ it is impossible to entrain firing with $f<F$. Conversely, with $g_e = 0$, it is impossible to entrain for $f>F$, and increasing $g_i$ strongly reduces the lower frequency limit of entrainment (Fig. 6c,d).

Since physiologically, entrainment must occur in the face of considerable noise, we also investigated the effect of adding noise

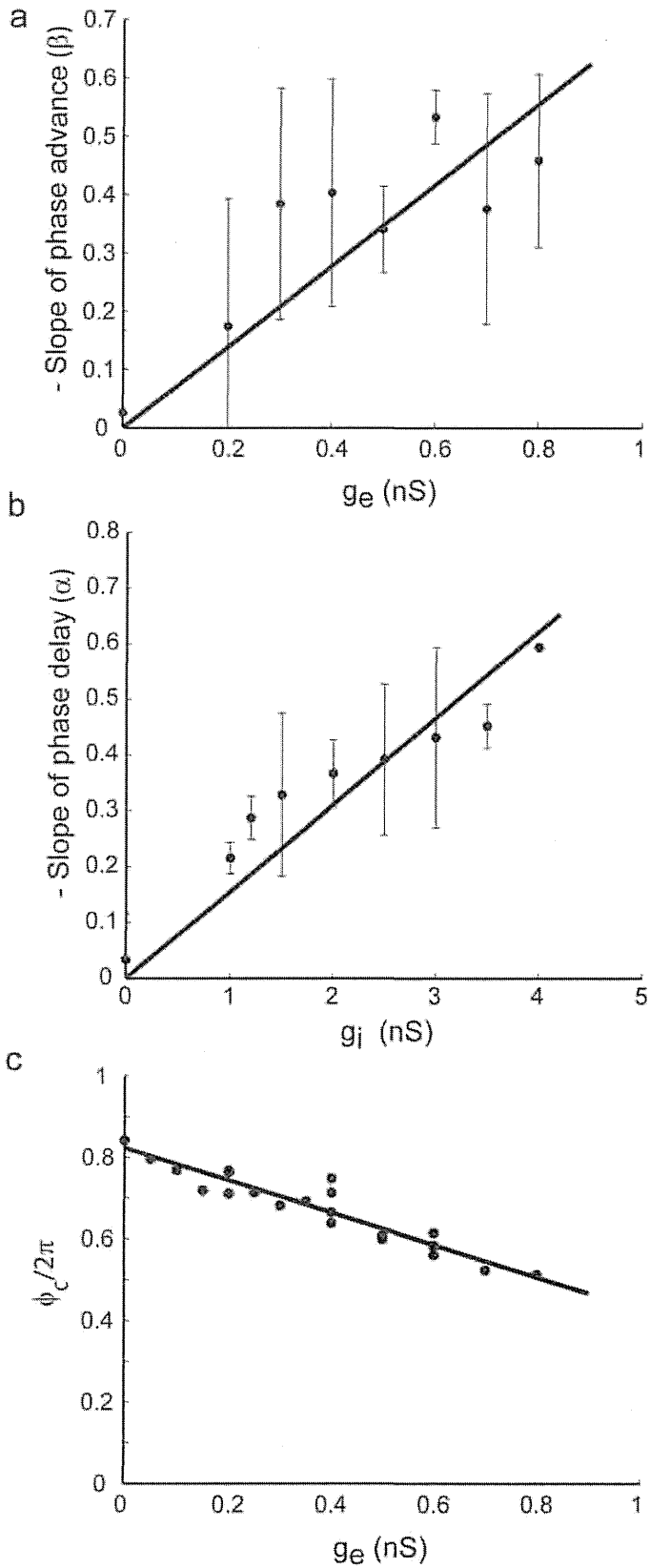
a
- Slope of phase advance (β)
0.7
0.6
0.5
0.4
0.3
0.2
0.1
0
0
0.2
0.4
0.6
0.8
1
$g_e$ (nS)
b
- Slope of phase delay (α)
0.8
0.7
0.6
0.5
0.4
0.3
0.2
0.1
0
0
1
2
3
4
5
$g_i$ (nS)
c
$\phi_c/2\pi$
1
0.8
0.6
0.4
0.2
0
0
0.2
0.4
0.6
0.8
1
$g_e$ (nS)

**Figure 3. SPRF parameters depend on the strength of synaptic perturbation in a simple manner.** a. Dependence of the phase advance slope ($-\beta$) on the gap-junctional conductance (for $g_i = 1.5$ nS). Data pooled from 120 measurements in 10 cells. b. Dependence of the phase delay slope ($-\alpha$) on $g_i$. Data from 43 measurements in 7 cells. c. Dependence of the critical phase at which delay switches to advance ($\phi_c$) on the gap-junctional conductance $g_e$ in one cell.
doi:10.1371/journal.pcbi.1000951.g003

to the phase map. It is possible to define stochastic bifurcation points of the map $F$, at which there is a qualitative change in the nature of the stochastic dynamics. These points coincide with the deterministic bifurcation frequencies [32] for $\sigma = 0$ (see Methods for details). We examined the frequency extents of this kind of stochastic entrainment at different noise levels (Fig. 6b–d). In all cases, increasing the noise in the phase shrinks the region of entrainment. For $\sigma = 0.1$ rad/$2\pi$, which was a typical noise level in these cells *in vitro*, the area of stochastic entrainment shrank to a third or less of the noise-free case. This noise-induced distortion is not symmetrical in the frequency axis. For example, Fig. 6d shows that in the absence of electrical coupling, the lower frequency limit of entrainment was highly susceptible to noise while the upper limit was not. The greater the level of electrical coupling ($g_e$), the more the upper limit was reduced by noise.

The SPRF makes several predictions. First, FS cells receiving purely electrical synaptic input will synchronize effectively when driven at frequencies higher than $F$. Higher frequencies can be followed with stronger electrical input. Second, cells will synchronize to purely inhibitory input at frequencies lower than $F$, and stronger inhibition allows lower frequencies to be followed. Third, combined electrical and inhibitory input allows cells to synchronize to frequencies both above and below their unperturbed frequency. Although noise diminishes the frequency band of synchronization, sometimes asymmetrically, these conclusions remain valid in the presence of noise. For typical strengths of combined electrical-inhibitory synaptic connections, 20 Hz or greater bandwidths of stochastic synchronization persist even in quite high levels of noise ($\sigma = 0.1$).

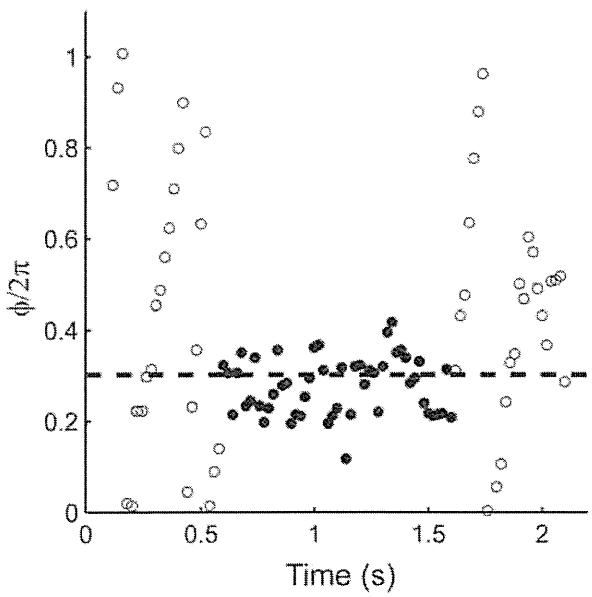


**Figure 4. Entrainment of firing to a periodic conductance input.** An example of a stroboscopic plot of the phase of a neuron, observed in phase with stimulation by a compound synaptic-like conductance of ($F = 56$ Hz, $f = 50$ Hz, $g_e = 750$ pS and $g_i = 3$ nS). The conductance pulses are applied during the period indicated by filled circles. Dashed line indicates the equilibrium solution of Eq. 2 for this cell.
doi:10.1371/journal.pcbi.1000951.g004

## Discussion

### Measuring the effect of synaptic conductance on phase of periodic firing

A number of previous theoretical and experimental studies have examined the phase-resetting properties of cortical neurons. Ermentrout and Kopell developed a theoretical approach to calculate what they termed the "synaptic interaction function" based on phase response curves and the assumption of weak coupling [33]. Reyes and Fetz (1993) stimulated synaptic inputs to regularly-firing pyramidal neurons to measure the phase resetting produced by EPSPs [34], while Stoop et al. (2000) used similar measurements to predict input frequency regions for entrainment and chaos [35]. Netoff et al. used dynamic-clamp to measure phase-resetting (or spike-time response curves) by artificial excitatory or inhibitory conductances in excitatory stellate cells of medial entorhinal cortex, and oriens-lacunosum-molecular interneurons in the CA1 region of hippocampus [36], and were able to demonstrate synchronization in pairs of neurons connected by artificial conductances mimicking synaptic connections, or between biological neurons and simulated neurons. In fast-spiking inhibitory cells, Mancilla et al. (2007) measured phase-resetting relationships for small current pulses (weak coupling) and showed that they could account quite well for synchronization of pairs of gap-junction coupled FS cells, both experimentally and in a biophysical model of FS neurons [37]. In this paper, we go further, by using conductance injection (dynamic clamp) to reproduce the combined effect of gap-junctional and strong synaptic connections, and using this to predict the resulting synchronized frequency bands, and their dependence on synaptic strength, including the effect of noise in the synaptic phase-resetting function on synchronization.

The conductance pulses which we have used are based on the physiological properties of the synaptic connections between FS neurons. In FS neurons of a basket morphology, APs initiate in the axon [38] arising usually from a proximal dendrite, [39] and receive many of their inhibitory connections and gap junctions from other fast-spiking interneurons perisomatically [14]. Thus, dynamic clamp recordings at the soma should provide a reasonably realistic simulation of the natural gap-junctional and fast inhibitory input.

In order to carry out this analysis, we have made the approximation that, between spikes, the presynaptic voltage of the gap-junctional input was held at a resting potential of $-70$ mV, . In other words, we have focused on the effect of gap-junctional current flow associated with the discrete event of the presynaptic spike. This approach does not take account of the way in which presynaptic membrane potential would gradually depolarize between spikes, if firing periodically. We have also ignored the two-way nature of coupling between cell pairs. In other words we model entrainment of one cell by another, rather than synchronization of a symmetrical coupled pair. Although both electrical and inhibitory coupling can often be asymmetrical [13,40], they may also be quite symmetrical. However, the entrainment studied here models the situation where the presynaptic cell is already imperturbably-driven as part of a strong synchronously-firing assembly of FS neurons, so that the phase and

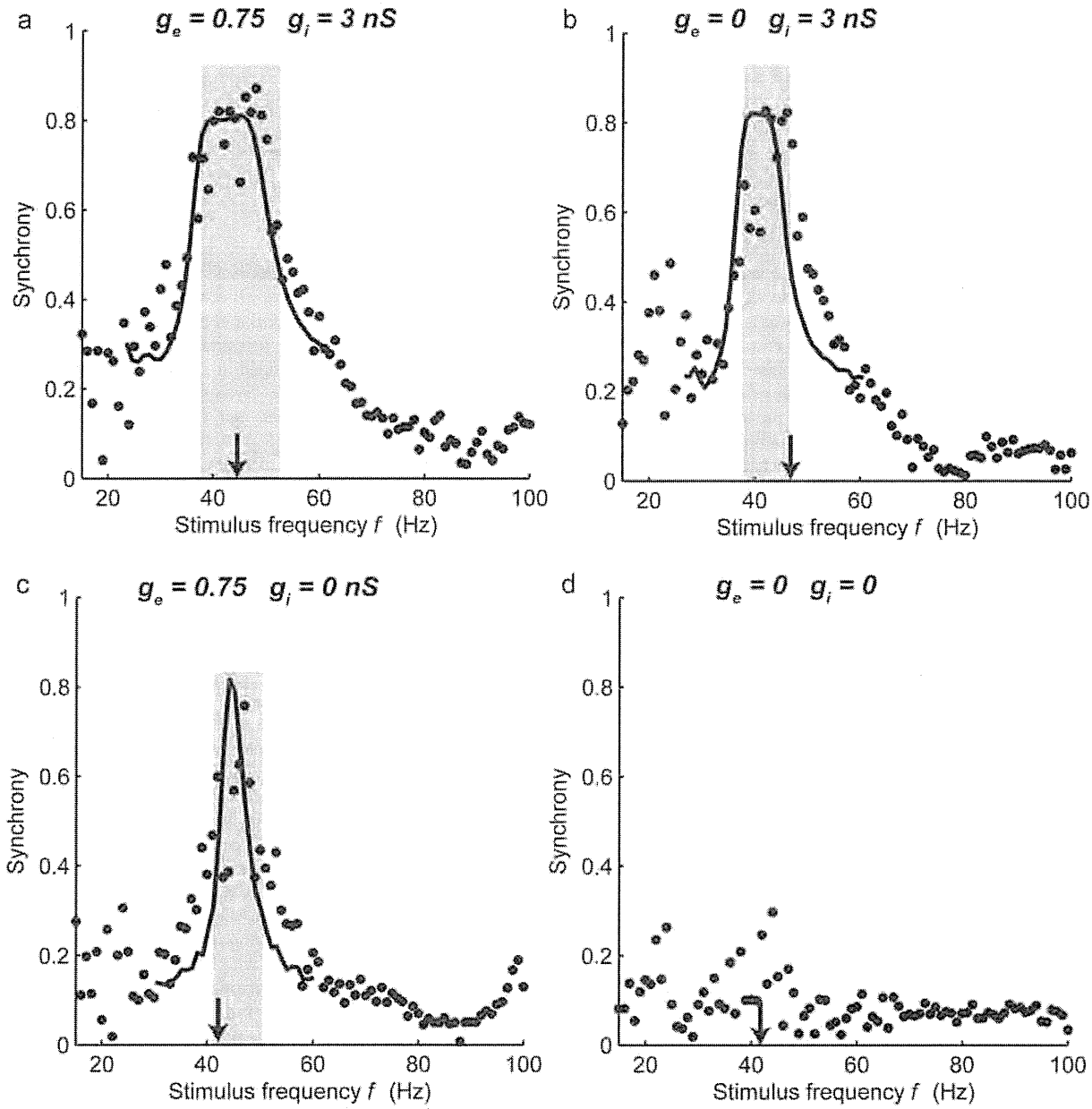


**Figure 5. Frequency dependence of entrainment.** The synchrony measure $S$ (see Methods) is plotted as a function of the frequency of the entraining input. Conductance values as shown. a) compound gap-junctional/inhibitory input. b) pure inhibitory input. c) pure gap-junctional input. d) random level of synchrony in the absence of conductance input. Arrowheads indicate the natural firing frequency $F$ in the absence of perturbations, and gray regions indicate the frequency bands of 1:1 synchronization predicted by the measured SPRF. Solid curves in (a)–(c) show the calculated steady-state synchrony of the fitted noisy SPRF model.
doi:10.1371/journal.pcbi.1000951.g005

frequency of its firing will be clamped to that of its predominant input. Thus, the SPRF that we measure should be an effective model for describing recruitment of new cells to such a synchronous assembly.

It is expected that the preferred firing frequency $F$ of the postsynaptic cell may also affect the form of the SPRF, since the timing of intrinsic ion channel kinetics will shift relative to phase as the cycle length changes. In a few experiments where we were able to address this issue, we indeed found evidence of a change in the parameters of the SPRF model. $a$, the dependence of phase delay on $g_i$, increased quite strongly as firing frequency increased, and $\phi_c$ shifted earlier in the cycle as firing frequency increased. The dependence of $b$ and $d$ on firing frequency was not marked. The relatively strong effect on $a$ may partly reflect the long duration of the IPSP conductance relative to the period of the cycle.

## The synaptic phase-resetting function

The synaptic phase-resetting function, or SPRF, for compound input was distinguished by the following features: an extremely abrupt midcycle switch from phase delay to phase advance, which shifted weakly towards the early part of the cycle as the strength of

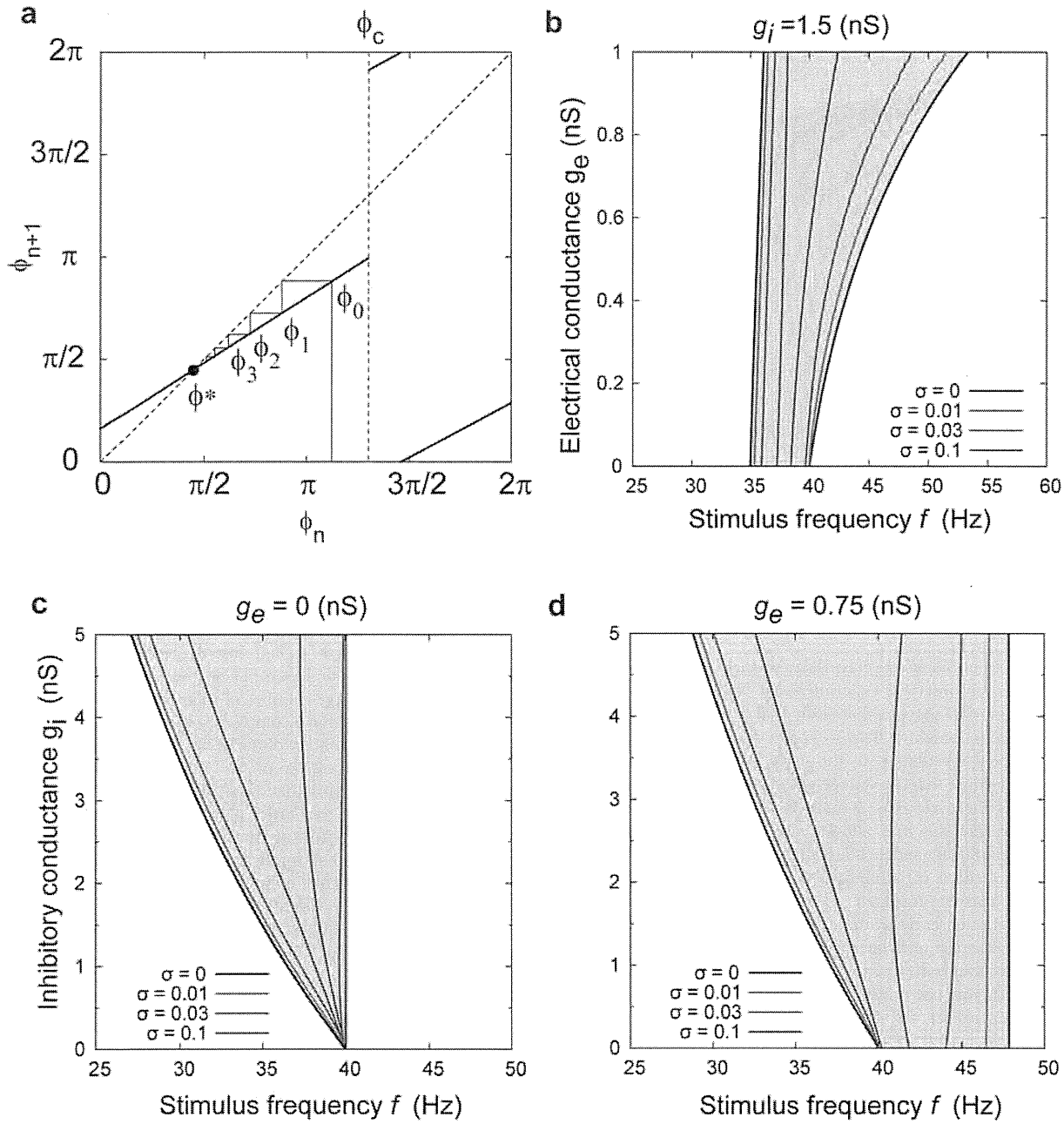


**Figure 6. Bifurcation analysis of frequency bands of synchronization.** a) piecewise linear map between phase at stimulus *n* and phase at stimulus *n+1*. The point $\varphi^*$ on the diagonal is a stable fixed point of the map, as illustrated by the converging orbit $\varphi_1$, $\varphi_2$, ... showing that 1:1 entrainment occurs at this stimulus frequency. b) bifurcation points of 1:1 entrainment in the $g_e$, *f* plane, $g_i = 1.5$ nS. 1:1 entrainment occurs in the gray regions. $\sigma = 0$, deterministic case. For $\sigma > 0$, stochastic bifurcation points with added Gaussian noise in the phase (see text). c) synchronization region in the $g_e$, *f* plane, with $g_e = 0$. (d) as in (b), with $g_e = 0.75$ nS. Raising $g_e$ strongly increases the upper frequency limit of entrainment, and weakly increases the lower limit. Noise shrinks the stochastic synchronization region. Parameters: $a = 0.12$/nS, $b = 0.625$/nS, $c = 0.8*2\pi$ rad, $d = 0.2*2\pi$ rad/nS.
doi:10.1371/journal.pcbi.1000951.g006

electrical coupling was increased; amplification of the phase delay region by increasing inhibition; and amplification of the phase advance region by increasing gap-junctional coupling. We found that these qualitative features were also present in a biophysical model of firing in fast-spiking cells [41] (see Methods), incorporating voltage-gated sodium, Kv1.3 and Kv3.1/3.2 potassium channels, and stimulated with exactly the same inputs as used experimentally (Fig. 7). In this fully-deterministic model, we also observed a very fine local structure of fluctuations around the main relationship, particularly in the phase delay. Despite these qualitative similarities between the model and experimental results, there were also major differences. In experiments, phase advance was produced exclusively by gap-junctional conductance and phase delay exclusively by inhibition, while in the model, gap-